COMPUTER SIMULATION OF ADAPTIVE OPTICAL SYSTEMS

W. P. Brown, Jr.

Hughes Research Laboratories

Prepared for:

Naval Surface Weapons Center

September 1975

DISCLAIMER NOTICE

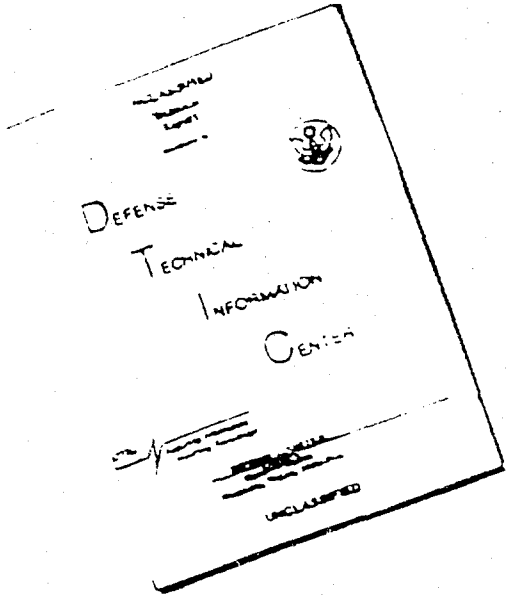

THIS DOCUMENT IS BEST QUALITY AVAILABLE. THE COPY FURNISHED TO DTIC CONTAINED A SIGNIFICANT NUMBER OF PAGES WHICH DO NOT REPRODUCE LEGIBLY.

COMPUTER SIMULATION OF ADAPTIVE OPTICAL SYSTEMS

W. P. BROWN, JR.

HUGHES RESEARCH LABORATORIES
3011 MALIBU CANYON ROAD
MALIBU, CALIFORNIA 90265

SEPTEMBER 1975

CONTRACT N60921-74-C-0249
FINAL TECHNICAL REPORT
FOR PERIOD 25 MARCH 1974 THROUGH 24 OCTOBER 1974

SPONSORED BY
NAVAL SURFACE WEAPONS CENTER
WHITE OAK
SILVER SPRING, MD 20910

UNCLASSIFIED

SECURITY CLASSIFICATION OF THIS PAGE (When Data Entered)

REPORT DOCUMENTATION PAGE		READ INSTRUCTIONS BEFORE COMPLETING FORM
1 REPORT NUMBER	2 GOVT ACCESSION NO	3 RECIPIENT'S CATALOG NUMBER
4 TITLE (and Subtitle) Computer Simulation of Adaptive Optical Systems		5 TYPE OF REPORT & PERIOD COVERED Final Technical Report 25 Mar 1974-24 Oct 1974
		6 PERFORMING ORG REPORT NUMBER
7 AUTHOR(s) W. P. Brown		8 CONTRACT OR GRANT NUMBER(s) N60921-74-C-0249
9 PERFORMING ORGANIZATION NAME AND ADDRESS Hughes Research Laboratories 3011 Malibu Canyon Road Malibu, California 90265		10 PROGRAM ELEMENT, PROJECT, TASK AREA & WORK UNIT NUMBERS
11 CONTROLLING OFFICE NAME AND ADDRESS Naval Surface Weapons Center White Oak Silver Spring, Maryland 20910		12 REPORT DATE July 1975
		13 NUMBER OF PAGES 65
14 MONITORING AGENCY NAME & ADDRESS (if different from Controlling Office)		15 SECURITY CLASS (of this report) Unclassified
		15a DECLASSIFICATION/DOWNGRADING SCHEDULE

16 DISTRIBUTION STATEMENT (of this Report)

Approved for public release; distribution unlimited.

17 DISTRIBUTION STATEMENT (of the abstract entered in Block 20, if different from Report)

18 SUPPLEMENTARY NOTES

19 KEY WORDS (Continue on reverse side if necessary and identify by block number)

Adaptive Optics
Turbulence
Thermal Blooming
Deformable Mirrors
Phase Compensation

20 ABSTRACT (Continue on reverse side if necessary and identify by block number)

In this report we discuss adaptive phase compensation for the effects of turbulence and thermal blooming. Closed-loop systems employing both outgoing-wave and return-wave control algorithms are considered, although we have obtained from quantitative estimates of system performance only for the return wave-type of system. On the basis of results obtained from a computer simulation of such systems, we conclude that

DD FORM 1 JAN 73 1473 EDITION OF 1 NOV 65 IS OBSOLETE

UNCLASSIFIED

SECURITY CLASSIFICATION OF THIS PAGE (When Data Entered)

20. ABSTRACT (continued)

adaptive optical systems employing a return-wave control policy will yield only limited compensation for the effects of cw thermal blooming unless the target has glints that are significantly smaller than the diffraction-limited width of the beam. We explain this in terms of an isoplanatic effect, in which the phase information returned from the glint is garbled by virtue of its finite extent. In contrast to the cw thermal blooming results, we find that return-wave systems are much less sensitive to glint size for turbulence and multipulse thermal blooming compensation (70 to 90% of free-space peak irradiance restored typically in the case of turbulence compensation and a factor of two to three increase in target irradiance in the case of multipulse thermal blooming). Analytical and computer simulation results have also been obtained for the dependence of mirror fit on the number of mirror actuators.

SUMMARY

In this report we discuss adaptive phase compensation for the effects of turbulence and thermal blooming. Closed-loop systems employing both outgoing-wave and return-wave control algorithms are considered, although we have obtained quantitative estimates of system performance only for the return wave-type of system. On the basis of results obtained from a computer simulation of such systems, we conclude that adaptive optical systems employing a return-wave control policy will yield only limited compensation for the effects of cw thermal blooming unless the target has glints that are significantly smaller than the diffraction-limited width of the beam. We explain this in terms of an isoplanatic effect, in which the phase information returned from the glint is garbled by virtue of its finite extent. In contrast to the cw thermal blooming results, we find that return-wave systems are much less sensitive to glint size for turbulence and multipulse thermal blooming compensation (70 to 90% of free-space peak irradiance restored typically in the case of turbulence compensation and a factor of two to three increase in target irradiance in the case of multipulse thermal blooming). Analytical and computer simulation results have also been obtained for the dependence of mirror fit on the number of mirror actuators.

TABLE OF CONTENTS

LIST OF FIGURES

I. INTRODUCTION

The principal objective of most high energy laser systems is to achieve the maximum possible irradiance at a distant target. Under ideal conditions the maximum irradiance is determined by free-space diffraction effects. In practice, however, this ideal state is seldom realized. We must contend additionally with wave distortions introduced by the laser device, by the optical train and by medium inhomogeneities in the path between the transmitter aperture and the target. In each case the distortion is caused largely by path length errors that introduce phase aberrations. In this report, we consider the improvement in beam quality attainable by adaptive optical systems that introduce a compensating phase distribution which tends to cancel the errors introduced by the phase aberrations. The compensating phase distribution is assumed to be generated by a corrector mirror located in the optical train; e.g., a segmented or deformable mirror located just before the output telescope. Furthermore, we are concerned primarily with closed-loop systems that obtain the requisite phase information via the energy returned from the target.

The principal objective of these studies has been to determine the effectiveness of closed-loop adaptive optical systems in compensating for the effects of turbulence and thermal blooming. The effects of device distortion and optical train errors were not considered but could easily be included in the formalism developed here if the nature of these errors was specified (e.g., the spatial and temporal spectrum of the errors).

To obtain quantitative estimates of the degree of compensation achievable with closed-loop adaptive optical systems, we have developed a computer model of such systems. The model includes a servo system simulator, a corrector

mirror simulator, a propagation simulator and a target simulator. The propagation simulator utilizes a propagation algorithm that accurately models the optical distortions introduced by atmospheric turbulence and thermal blooming.

Before proceeding to the discussion of the simulation and the results obtained therefrom, we discuss in Section II some of the fundamentals of adaptive phase compensation for the effects of medium inhomogeneities. This is followed in Section III by a discussion of the details of the computer simulation that has been developed on this contract. Results obtained from the computer simulation and from analysis are then given in Section IV. The conclusions that we have reached based on this work and our recommendations for additional work on the computer simulation of closed-loop adaptive optical systems are discussed in Section V.

II. FUNDAMENTALS OF ADAPTIVE COMPENSATION FOR MEDIUM INHOMOGENEITIES

In this section we discuss the basic principles and fundamental limitations of two broad classes of adaptive optical techniques for compensating for medium inhomogeneities caused by thermal blooming and turbulence. The two classes of techniques to be considered are (1) return-wave algorithms in which the phase corrections are determined from direct measurements of the returned field (e.g., the phase conjugate technique) or by a maximization of some functional of the irradiance distribution obtained by imaging the target (e.g., maximization of the energy through a pinhole for a point glint target or maximizing the "sharpness" of an image of an extended target) and (2) outgoing-wave multidither algorithms in which the phase corrections are determined by maximizing the integrated irradiance of the field reflected from the target and intercepted by a detector located in the vicinity of the transmitter (e.g., the sinusoidal multidither technique used in the 19-element experimental COAT system constructed by HRL). In comparing these techniques we will assume that the adaptive system responds instantaneously to changes in the state of the medium caused by thermal blooming and turbulence. In effect, this assumption linearizes the propagation phenomenon since we then do not have to be concerned with the local effect (in time) of the phase correction on the medium. This idealization should apply as long as the response time of the adaptive system is short compared to the time constants for the thermal blooming.

For each class of technique we are interested in determining the effect of the phase corrections on the field at the target. This field can be derived, in general, from a scalar function u which satisfies the relation

$$u(\underline{x}'') = \int d\underline{x}' \; u_s(\underline{x}') \; G(\underline{x}'', \underline{x}') \qquad (2.1)$$

where u_s is the field at the transmitter aperture and G is the Green's function for the inhomogeneous medium; i.e., $G(\underline{x}'', \underline{x}')$ is a scalar function from which we can derive the field at $\underline{x}''$ excited by a point source located at $\underline{x}'$. It follows from Eq. (2.1) that the field at a point $\underline{x}$ caused by the reflection of the transmitted wave from a point target at $\underline{x}''$ is

$$u_R(\underline{x}) = G(\underline{x}, \underline{x}'') \int d\underline{x}' \, u_s(\underline{x}') \, G(\underline{x}'', \underline{x}') \qquad (2.2)$$

Likewise, the field at $\underline{x}$ caused by the reflection of the transmitted wave from an extended target having the complex reflectivity function $\rho(\underline{x}'')$ is

$$u_R(\underline{x}) = \int d\underline{x}'' \, \rho(\underline{x}'') \, G(\underline{x}, \underline{x}'') \int d\underline{x}' \, u_s(\underline{x}') \, G(\underline{x}'', \underline{x}') \qquad (2.3)$$

Equations (2.2) and (2.3) are the fundamental relations upon which we shall base the discussion of the two classes of adaptive compensation techniques.

2.1 Return-Wave Algorithms

All return-wave algorithms have the property that the phase correction applied to the transmitted wave is the conjugate of the phase of the field returned from the target. This is true not only for the explicit phase conjugate technique but also for the case in which a functional of the irradiance distribution obtained by imaging the target is maximized. Muller and Buffington have proved this for an incoherent imaging system that maximizes the "sharpness" of an image of an extended target.[1] It is also easily proved for a coherent system that maximizes the energy from a point glint target through a pinhole in the image plane of a receiving aperture. In this case the field at the receiving aperture is proportional to $G(\underline{x}, \underline{x}'')$ which can be expressed in the form

$$G(\underline{x},\underline{x}'') = A(\underline{x},\underline{x}'') \exp\left(i\phi(\underline{x},\underline{x}')\right) G_o(\underline{x},\underline{x}'') \qquad (2.4)$$

where G_o is the free space Green's function and A and ϕ are the amplitude and phase variations caused by the medium inhomogeneities. After the introduction of a compensating phase distribution $\phi_c(\underline{x})$ in the aperture plane, the field in the image plane of a lens used to image the point $\underline{x}''$ is

$$u_{image}(\underline{x}_i) = \int d\underline{x}\, A(\underline{x},\underline{x}'') \exp\left[i\left(\phi(\underline{x},\underline{x}'') + \phi_c(\underline{x})\right)\right] \exp\left(-i\, k\, \frac{\underline{x}\cdot\underline{x}_i}{f}\right) \qquad (2.5)$$

where f is the distance from the aperture plane to the image plane of the lens. Hence the irradiance through a pinhole located at $\underline{x}_i = 0$ is

$$I_{image}(0) = \left| \int d\underline{x}\, A(\underline{x},\underline{x}'') \exp\left[i\left(\phi(\underline{x},\underline{x}'') + \phi_c(\underline{x})\right)\right] \right|^2 \qquad (2.6)$$

and we note that since A is positive the maximum value of I_{image} is attained under $\phi_c = -\phi$, i.e., when the compensating phase distribution is the conjugate of the atmospheric phase distortions.

Another important general property of return-wave algorithms is that they are based on the fact that Green's function $G(\underline{x},\underline{x}'')$ satisfies the reciprocity relation (see Appendix A for a discussion of reciprocity)

$$G(\underline{x},\underline{x}') = G(\underline{x}',\underline{x}) \qquad (2.7)$$

which means that the field observed at a point $\underline{x}$ from a source at a point $\underline{x}'$ is the same as the field observed at $\underline{x}'$ from a source at $\underline{x}$. Equation (2.7) applies even though the intervening space between $\underline{x}$ and $\underline{x}'$ is inhomogeneous. The only restriction is that we assume that the propagation is linear, which it is under the assumption we have made.

Let us now consider the effect of introducing as a phase correction the conjugate of the phase of the field returned from the target. For a point target we note from Eq. (2.2) that the returned field is proportional to $G(\underline{x},\underline{x}'')$ and thus that the phase correction applied by a return-wave system is $-\phi(\underline{x},\underline{x}'')$. The field at the target is then given by

$$u(\underline{x}'') = \int d\underline{x}' \, u_s(\underline{x}') \exp\left(-i\phi(\underline{x}',\underline{x}'')\right) G(\underline{x}'',\underline{x}')$$

$$= \int d\underline{x}' \, u_s(\underline{x}') \, A(\underline{x}'',\underline{x}') \, G_o(\underline{x}'',\underline{x}') \, , \qquad (2.8)$$

where we have used Eq. (2.4) to express G in terms of A,ϕ and the free space Green's function G_o and have used the reciprocity relation given in Eq. (2.7) to eliminate the phase terms $\phi(\underline{x}',\underline{x}'')$ and $\phi(\underline{x}'',\underline{x}')$, i.e.,

$$-\phi(\underline{x}',\underline{x}'') + \phi(\underline{x}'',\underline{x}') = 0. \qquad (2.9)$$

The result in Eq. (2.8) indicates that return-wave algorithms yield good compensation in the case of point glint targets as long as the amplitude factor A does not vary significantly across the transmitting aperture. Appreciable variation in A across the aperture will lead to an effective apodization of the aperture and will tend to increase the sidelobe level and the beamwidth of the transmitted energy.

For an extended target the return field is given in Eq. (2.3), which we repeat here for convenience

$$u_R(\underline{x}) = \int d\underline{x}'' \, \rho(\underline{x}'') \, G(\underline{x},\underline{x}'') \int d\underline{x}' \, u_s(\underline{x}') \, G(\underline{x}'',\underline{x}'). \qquad (2.3)$$

If the target reflectivity function is simply a collection of zero width glints located over an extended region, it can be shown that the previous point target analysis applies and we conclude that a return-wave system will yield good compensation for such targets as long as the amplitude factor A does not

vary too much. More realistically, however, the target glints have finite extent and the previous analysis does not apply. For example, consider the case where there is a single glint of finite extent. Moreover, let us assume that the range of $\rho(\underline{x}'')$ is small compared to that of the incident field from the transmitter. In this case the return field can be approximated by

$$u_R(\underline{x}) \sim \left(\int d\underline{x}'' \; \rho(\underline{x}'') \; G(\underline{x}, \underline{x}'') \right) \left(\int d\underline{x}' \; u_s(\underline{x}') \; G(\underline{x}_o'', \underline{x}') \right) \quad (2.10)$$

where $\underline{x}_o''$ is the point where the reflectivity function $\rho(\underline{x}'')$ has its maximum value. Hence, a return-wave algorithm will apply as a correction the conjugate of the phase of the factor

$$\int d\underline{x}'' \; \rho(\underline{x}'') \; G(\underline{x}, \underline{x}'') \quad (2.11)$$

which is a weighted average of the Green's function over the domain of the reflectivity function $\rho(\underline{x}'')$. This phase correction policy will yield good compensation only if the phase of $G(\underline{x}, \underline{x}'')$ does not vary appreciably over the range of ρ. Otherwise, the conjugate phase is garbled by the interference between the returns from the different parts of the domain of $\rho(\underline{x}'')$. The negative of the phase of the factor in Eq. (2.11) will then not exactly cancel the phase $\phi(\underline{x}_o'', \underline{x}')$ of $G(\underline{x}_o'', \underline{x}')$ and the compensation will be degraded. An example of this type of problem is provided by a similar situation in adaptive imaging through inhomogeneous media. It is well known that good compensated imaging can be obtained only if the object lies within an isoplanatic region, which has the property that the phase distortion $\phi(\underline{x}, \underline{x}'')$ introduced on a point source field radiated from a point $\underline{x}''$ on the object to a point $\underline{x}$ in the receiving aperture is nearly the same for points $\underline{x}''$ within this region.

The importance of the isoplanatic problem in return-wave adaptive compensation systems will depend largely on the

nature of the target reflectivity function and on the source of the medium inhomogeneity. In our computer simulations of phase conjugate compensation for the effects of thermal blooming we have assumed that the target glints extend over an area approximately equal to the diffraction-limited size of the transmitted beam. Under these conditions, we have found that the compensation achieved tends to be disappointingly small and we attribute this to the above discussed isoplanatic problem. Numerical problems associated with the attendant wide-angle scattering have prevented us thus far from simulating glints that are significantly smaller than the diffraction-limited spot.

For turbulence compensation problems we can readily estimate the size of the isoplanatic region. Its linear extent D_{iso} is roughly equal to the distance between two points on the target at which the mean square difference in the phase of a point source field radiated from a point $\underline{x}$ in the transmitter aperture is unity. Assuming Kolmogorov turbulence, we obtain the relation

$$D_{iso} = (1.1\, k^2\, C_N^2\, f)^{-3/5} \qquad (2.12)$$

where C_N^2 is the index structure constant, k is the wavenumber $2\pi/\lambda$ and f is the distance to the target. In the computer simulations of phase conjugate compensation for the effects of turbulence, we have generally obtained good correction with glints that extend over a diffraction-limited spot area. This is consistent with the fact that the isoplanatic region associated with the turbulent inhomogeneities was larger than the diffraction-limited spot in these runs. For instance, the diameter of the diffraction-limited spot obtained with a 70 cm, 10.6 μm laser beam focussed at a range of 2 km is approximately 3 cm ($f\lambda/D$), whereas the diameter of the isoplanatic region obtained from Eq. (2.12) is in the range $6 \leq D_{iso} \leq 28$ cm for the range of index structure constant

values used in the simulations (5×10^{-16} cm$^{-2/3} \leq C_N^2 \leq 6 \times 10^{-15}$ cm$^{-2/3}$).

2.2 Outgoing-Wave Multidither Algorithms

Outgoing-wave multidither algorithms adjust the phase of the transmitted wave to maximize the irradiance of the field reflected from the target. To accomplish this, the phase of the transmitted field is dithered in a distinct set of spatial-temporal modes. The resulting modulations on the irradiance of the field reflected from the target are then detected and sent to a servo system that tends to set the corrector mirror actuators so as to drive the modulations to zero. In doing so, the servo system sets the actuators in the positions where the derivatives of the detected signal with respect to the phase correction are zero, which is the condition for a maximum (the fact that it is a maximum and not a minimum can be determined by the phase of the signal).

The detector current in an outgoing-wave multidither system is proportional to integral I of the irradiance of the field u_R reflected from the target. For a point target, we obtain from Eq. (2.2)

$$I = c \int d\underline{x} \, |G(\underline{x},\underline{x}'')|^2 \tag{2.13}$$

where c is the irradiance of the transmitted field at the target

$$c = \left| \int d\underline{x}' \, u_g(\underline{x}') \, G(\underline{x},\underline{x}') \right|^2 \tag{2.14}$$

Note that the integral in Eq. (2.13) does not depend on the transmitter field u_g. Hence, a maximization of I with respect to the transmitter phase yields maximum irradiance at the target, as desired.

For extended targets the reflected field is given by Eq. (2.13). As in the case of return-wave algorithms, the above point target analysis applies if the target reflectivity function is simply a collection of zero width glints located over an extended region (with the difference that the receiver detector must now also be extended in order to achieve the desired maximization of the irradiance of the target). As an example of an extended target, we shall consider the case discussed in the return-wave algorithm discussion of Section 2.1; viz., a single glint of finite extent for which the range of the reflectivity function $\rho(\underline{x}'')$ is small compared to that of the incident field from the transmitter. In this case the return field can be expressed in the form given in Eq. (10) and the corresponding expression for the integrated irradiance returned from the target becomes

$$I = c \int d\underline{x} \left| \int d\underline{x}'' \, \rho(\underline{x}'') \, G(\underline{x},\underline{x}'') \right|^2 \qquad (2.15)$$

where c is again the irradiance of the transmitted field at the target. Although the field returned from the extended glint differs from that returned from the point glint, we note from Eq. (2.15) that a maximization of I again leads to a maximization of the irradiance at the target. As in the point target case, this occurs because the integral over $\underline{x}$ in Eq. (2.15) does not depend on the transmitter field u_s.

The above analysis indicates that, in contrast to return-wave algorithms, outgoing-wave multidither algorithms are relatively insensitive to target glint size. Of course, this is true only up to a point. If the range of the glint reflectivity function $\rho(\underline{x}'')$ is large compared to that of the field incident from the transmitter, the return field is approximately given by

$$u_R(\underline{x}) = \rho(\underline{x}_o'') \int d\underline{x}'' \, G(\underline{x},\underline{x}'') \int d\underline{x}' \, u_s(\underline{x}') \, G(\underline{x}'',\underline{x}'), \qquad (2.16)$$

and the integrated irradiance returned from the target becomes

$$I = |\rho(\underline{x}_o'')|^2 \int d\underline{x} \left| \int d\underline{x}'' \, G(\underline{x},\underline{x}'') \int d\underline{x} \, u_a(\underline{x}') \, G(\underline{x}'',\underline{x}') \right|^2 \tag{2.17}$$

Hence, in this case an outgoing-wave multidither system maximizes a complicated functional of the transmitter irradiance at the target instead of the transmitter irradiance itself and we should not expect to achieve good compensation (this behavior has been observed experimentally with the HRL 18-element multidither COAT system).

In summary, the results of this section and those of Section 2.1 indicate that: (1) both return-wave and outgoing-wave (multidither) phase compensation algorithms should yield good compensation for medium inhomogeneities for point glint targets; (2) return-wave algorithms are much more sensitive to glint size than outgoing-wave algorithms, especially in the case of thermal blooming compensation; and (3) when the size of the target glints significantly exceeds the size of the diffraction-limited focal spot of the transmitted field at the target, we do not expect the outgoing-wave multidither algorithm to work.

III. ADAPTIVE OPTICAL SYSTEM SIMULATION

3.1 Organization and Approach

The essential elements of the adaptive optics computer simulation are indicated in Fig. 3.1. The simulation contains computer routines that model the operation of an adaptive optical system consisting of a servo system and a corrector mirror. The effect of the atmosphere on the resulting laser beam propagation is modeled by a time-dependent propagation code that treats the effects of both turbulence and thermal blooming. The simulation models a closed-loop adaptive system in which the control information is provided by the detection of a return-wave reflected from the target. Propagation on the return path is modeled by a time-dependent linear propagation code, which includes the effects of the inhomogeneities caused by turbulence and the absorptive heating introduced by the high-power transmitted wave. The nature and current status of the various parts of the simulation are discussed in Sections 3.2 to 3.5.

As indicated above, we use a time-dependent propagation code to model the laser propagation on the outgoing and return paths. This differs from the approach taken by Herrmann and Bradley of Lincoln Laboratory who have used a cw code in their phase compensation studies.[2] It is admittedly true that the use of a time-dependent propagation code greatly increases the complexity and cost of the calculation but we have felt compelled to use this approach for two reasons. First, the time-dependent approach is closer to the physics of the striation that we are trying to simulate since we are primarily interested in adaptive optical systems that respond in a time short compared to the time it takes the atmosphere to change. Such adaptive systems perform an essentially instantaneous determination of the required phase front. Moreover, the determination

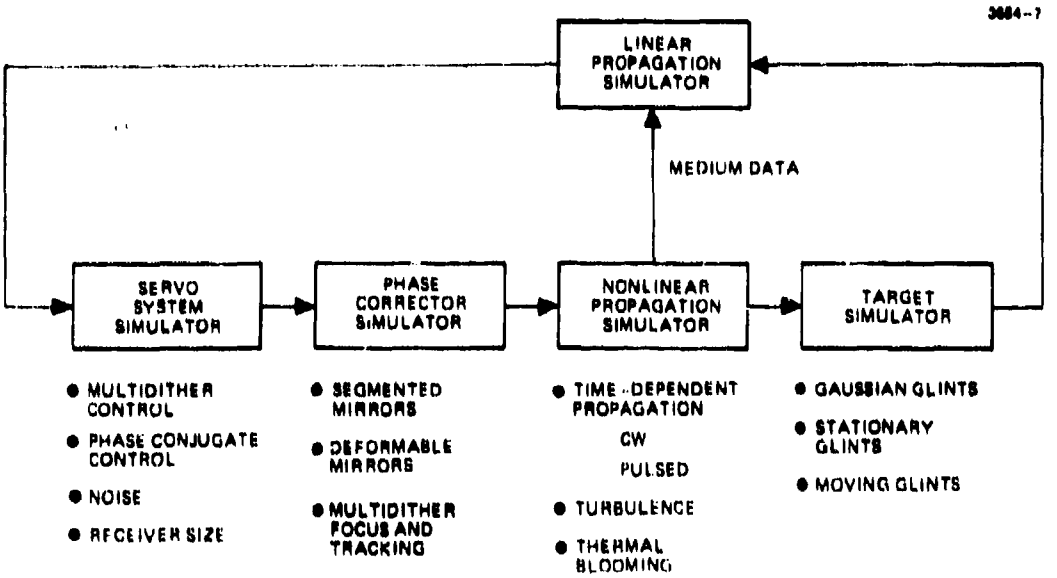

Fig. 3.1. Adaptive optical system simulation flow diagram.

is continuously updated as the medium changes, rather than to be put in and held fixed until a steady state is reached, as is implicitly assumed when a cw propagation code is used. The distinction between the time-dependent and cw approaches is especially important for the simulation of adaptive systems that employ return-wave algorithms. Whereas it can be argued that a cw code in conjunction with a maximization routine closely models the behavior of an adaptive optical system employing an outgoing-wave multidither algorithm, it does not appear possible to model return-wave systems with the cw approach since such systems do not explicitly maximize the irradiance on the target. Instead, as discussed in Section 2.1, they continuously set the phase of the transmitted wave equal to the conjugate of the phase of the field returned from the target. There does not appear to be any reason to expect that the final state reached by such a system can be obtained from a cw calculation or a sequence of such calculations.

The other reason for the use of a time-dependent propagation code in our studies is the desire to follow the time development of the correction process, especially in the case of adaptive systems employing outgoing-wave multidither control algorithms. As discussed in Section 2.2, an outgoing-wave multidither control system attempts to maximize the irradiance at the target at each instant. We wish to know if this instantaneous maximum control policy leads to a global maximum in the thermal blooming correction problem or, instead, yields a secondary maximum. This can be determined by comparing the maximum obtained with the time-dependent and the cw codes because the cw approach yields the global maximum.

The time-dependent propagation algorithm used in the simulation is basically a multi-pulse code in which the laser energy is propagated in a series of short pulses. The pulse length is assumed short enough that no heating occurs during the pulse. Furthermore, it is assumed that the heating caused by a pulse has reached a steady state by the time the

next pulse arrives. The term steady state is used here in the sense that all density gradients traveling at the sound velocity are assumed to have left the region occupied by the laser beam by the time the next pulse arrives. The only gradients present are those that are convected with the local crosswind velocity. Each pulse "sees" the medium created by the steady state heating of all previous pulses but is unaffected by its own heating. This model allows us to simulate either pulsed or cw propagation, depending on the time between pulses relative to the time it takes an air parcel to traverse the beam. CW propagation conditions are simulated by allowing significant overlap between the regions heated by successive pulses.

The time sequence of events in the simulation is shown in Fig. 3.2. First, a high-power pulse of laser energy is propagated to the target and the resulting change in the density of the air in the region occupied by the beam is calculated, taking into account the convective effect of the local crosswind velocity. It is assumed that the adaptive phase compensation is applied just prior to the firing of the next high-power laser pulse. Moreover, we are presently assuming that the adaptive optical system has infinite bandwidth so that it is able to determine and apply the phase correction instantaneously without any delay or time-averaging effects. The information required to determine the phase correction is obtained by transmitting a low-power reference pulse to the target and reflecting the same from the target. This reference pulse propagates through the medium that will be seen by the next high-power pulse and thus provides the necessary phase correction information. This process is then repeated for each subsequent high-power pulse.

With the exception of some runs in which the effect of the atmosphere was represented by a single phase screen in front of the transmitter, all of the data that have obtained to this date apply to the simulation of adaptive systems

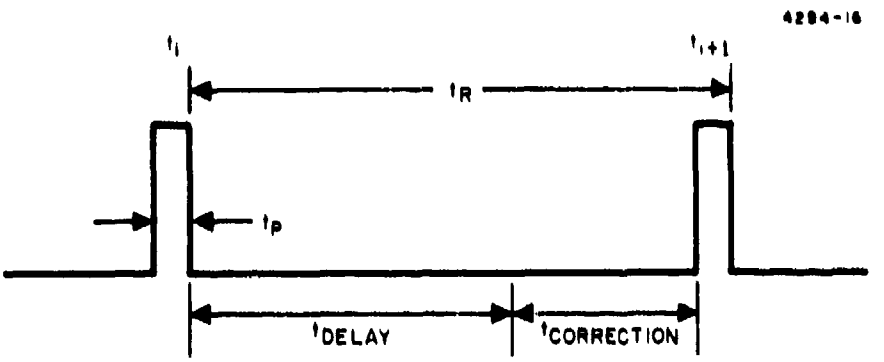

Fig. 3.2. Time sequence of events in multipulse adaptive optics simulation:

(1) No heating during a pulse ($t_p \ll t_{acoustic}$);

(2) Steady state heating for $t-t_i \leq t_{delay}$;

(3) Adaptive optics correction applied in the interval $t_{delay} < t-t_i < t_R$.

utilizing a return-wave control algorithm, i.e., systems that correct by inserting the conjugate of the phase of the wave returned from the target. The reason for this concentration on the phase conjugate simulation is simply that such simulations are significantly easier to implement and less costly to run than outgoing-wave simulations. The simulation of a return-wave system requires simply that we transmit a single low-power reference wave to the target and a single low-power reflected wave back to the transmitter aperture. The phase correction is then equated to the conjugate of the phase of the reflected field. In contrast, an accurate multidither simulation requires the sending and receiving of many low-power reference pulses for each high-power pulse. We must sample the modulations of the integrated irradiance of the target returns at a rate set by the highest dither frequency. For example, it was found in our earlier multidither servo system simulations that a sampling time increment of 5 μsec is required for an 18-channel system having an upper dither frequency of 32 kHz and an overall convergence time of 1 ms.[3] Hence, approximately 200 samples/convergence time were required in those simulations. It was practical to take 200 samples/convergence time in the earlier work because of the simplicity of the propagation model that was used. In the present case, however, the propagation model is quite complicated and relatively costly to run and thus it is clearly not practical to do an equivalent simulation.

At the outset of this contract we had planned to circumvent the multidither simulation problem as follows: (1) propagate a low-power reference pulse to the target; (2) propagate the associated low-power pulse reflected from the target back to the transmitter aperture; (3) use the calculated return wave to estimate the Green's function of the medium; (4) dither the phase of the reference pulse and calculate the resulting variations in the irradiance received

from the target, utilizing the Green's function information obtained previously (i.e., we did not plan to use the full propagation simulation every dither cycle, but rather intended to do this only once per high-power pulse); and (5) process the variations in received irradiance in a multidither servo simulator to determine the mirror actuator settings. During the course of the work on this contract, it became apparent, however, that such a simulation is an empty exercise because it does not simulate the desired behavior of an actual outgoing-wave multidither system in a thermal blooming situation. The problem is that the assumption that the Green's function can be determined from the return field reflected from the target is not valid in the thermal blooming problem unless the target is extremely small, in fact, unless it is nearly a point target. But it can be shown from the analysis in Section II that outgoing-wave multidither and return-wave adaptive optical systems both put in the conjugate phase when the target is a point target. Therefore, the simplified approach to multidither outlined above either yields results equivalent to those obtained with a return-wave algorithm (point glint) or yields results that are patently incorrect (extended glint).

We now think that the best way to simulate outgoing multidither adaptive systems is to use a function maximization routine in conjunction with the time-dependent propagation code. This is a modified version of the approach used by Herrmann and Bradley in their phase compensation studies. They have used a function maximization routine in conjunction with a cw propagation code. We recommend the use of a time-dependent code because it will allow us to determine directly whether or not the outgoing-wave multidither algorithm yields a truly global maximum and not just a secondary maximum.

3.2 Control System Simulation

As discussed in Section 3.1, we have primarily used a phase conjugate control policy in the computer studies of thermal blooming and turbulence compensation performed on this contract. Moreover, the phase conjugate control algorithm that we have used is particularly simple in that we have simply equated the phase of the transmitted wave to the conjugate of the phase of the wave returned from the target on a mesh point by mesh point basis. We have not taken into account the effect of the finite area of the phase detector and detector noise in these studies because we wished to establish an upper limit on the amount of correction that is achievable with a phase conjugate control algorithm and to avoid the problem of determining whether the particular detector configuration used is the optimum choice. For example, there is the question of how large to make the detectors. Should we use a collection of small point detectors or should we use larger detectors that yield spatially averaged phase estimators? The refinements in our present approach necessary to account for these effects are discussed below.

The phase detector can be represented as a finite aperture heterodyne detector, which performs a coherent summation of the return-wave field over the detector aperture, followed by a device that determines the phase of the detector output. The detector output is

$$i_{det} = \beta \int_{aperture} d\underline{x}\; u_R(\underline{x})\; u_{LO}^*(\underline{x}) + i_{noise} \qquad (3.1)$$

where β is a constant, u_R is the field returned from the target, u_{LO} is the local oscillator field, and i_{noise} is a shot noise current. Note that even in the absence of noise, a finite detector does not yield an exact measure of the

phase of the return-wave field but rather gives an average value determined by the integral in Eq. (3.1). The phase of the detector output is

$$\phi_{det} = \tan^{-1}\left[\frac{\tan\phi_S + \frac{A_N}{A_S}\frac{\sin\phi_N}{\cos\phi_S}}{1 + \frac{A_N}{A_S}\frac{\cos\phi_N}{\cos\phi_S}}\right] \tag{3.2}$$

where

$$\beta \int_{\text{aperture}} d\underline{x}\; u_R(\underline{x})\; u^*_{LO}(\underline{x}) \equiv A_S \exp(i\,\phi_S) \tag{3.3}$$

$$i_{noise} = A_N \exp(i\,\phi_N) \tag{3.4}$$

For shot noise-limited detection, the noise current in Eq. (3.4) is a gaussian random process and thus can be simulated by a gaussian random number generator. The mean square magnitude of these numbers is determined by the detector signal-to-noise ratio S/N

$$\langle A_N^2 \rangle = A_S^2 (S/N)^{-1} \tag{3.5}$$

For each return wave a finite set of phase samples can be determined from the relations given in Eqs. (3.2) through (3.5). The conjugate of these samples can then be used as inputs to the mirror simulator discussed in Section 3.3. The resulting phase-corrected wave is then transmitted to the target and a new return wave calculated. For point targets, the necessary phase correction is established by a single calculation of this type. Our experience indicates that this transmit-return wave calculation must be iterated four to five times in order to achieve convergence on a complex target, i.e., a target having more than one glint.

With regard to the question of how to simulate outgoing-wave multidither control algorithms we recommend, as mentioned in Section 3.1, that a function maximization routine be used in conjunction with a time-dependent propagation code (see Fig. 3.3 . The basis of this approach is the fact that an outgoing-wave multidither algorithm is a maximization process. It attempts to maximize the integrated irradiance of the field returned from the target. Hence the detector in Fig. 3.3 is represented in the simulation by an integration of the return irradiance over an area equal to that of the receiver being modeled. The maximization can be done with respect to any desired set of parameters that describe the state of the corrector mirror, e.g., the actuator position, the coefficients of a set of orthogonal polynomial such as Zernike functions, or the coefficients of some predicted set of correction functions (such as parabolic refocus adjustment plus a variable percentage of the phase distortion introduced in the first propagation step as implemented by Bradley and Herrmann).

3.3 Mirror Simulation

We have developed simulations of both segmented and deformable mirrors. The segmented mirror simulation is a relatively trivial exercise in that it simply consists in dividing the mirror mesh into a set of square-shaped zones within an outer circular boundary (see Fig. 3.4). The phase within each zone is assumed to be constant; i.e., the mirror consists of a set of flat segments.

In the deformable mirror simulation, it is assumed that the mirror is driven by actuators equi-spaced on a square array of mesh points. The fundamental problem is to find a relatively simple, low-cost method for calculating the mirror profile resulting from an arbitrary set of actuator displacements. It is not practical to use a sophisticated simulation

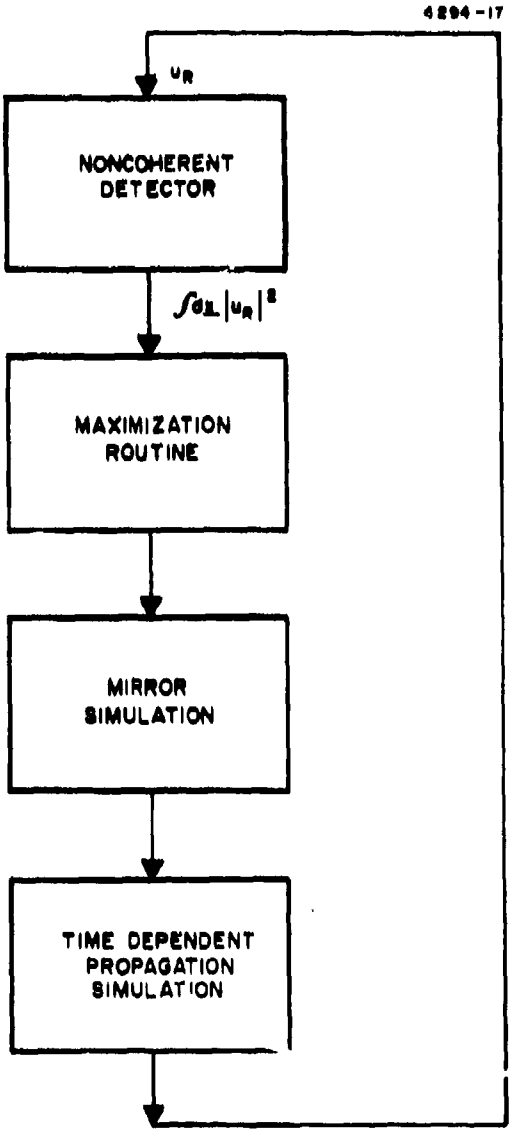

Fig. 3.3. Multidither control simulation.

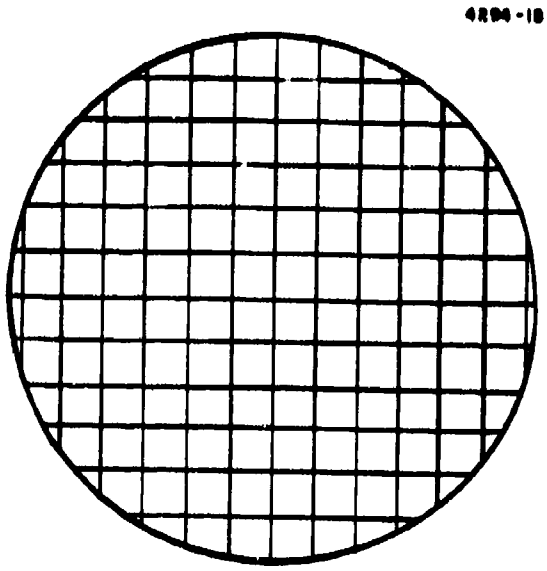

Fig. 3.4. Segmented circular mirror configuration.

such as the NASTRAN code in these studies. Instead, we have simplified the problem by assuming that thin plate theory is applicable, and that linear superposition holds. It is also assumed that the connection to the mirror from each actuator is effected at a single point (i.e., the actuators have zero width at the point of contact with the mirror) and that pure thrust without torque is transmitted. With these assumptions, the problem reduces to finding the mirror profile resulting when one actuator is raised unit height with all of the surrounding actuators held fixed at zero height. This is referred to as the unit profile. The total mirror profile at any instant is calculated by summing a set of unit profiles, each centered at one of the actuators and each weighted by the height of its associated actuator.

The detailed form of the unit profile depends on the actuator configuration. We have calculated unit profiles for deformable mirrors having 37, 57, and 97 actuators. In each case the unit profile is calculated as follows. First, we consider the mirror profile that results from the displacement of a single actuator at the center of a thin plate which is constrained only at a circular edge whose radius is large compared with the extent of the region occupied by the mirror. No other actuator constraints are assumed at this stage. We determine the profile from the following relation obtained from thin plate theory[4]

$$\text{displacement} \propto 5(a^2 - r^2) - 4r^2 \ln \frac{a}{r} \qquad (3.6)$$

where a is the distance to the edge of the plate and r is the distance from the central actuator to the point at which the displacement is measured.

For the profile in Eq. (3.6) the height at adjacent actuator positions is not zero when the central actuator is displaced. To determine the unit profile, we sum the

contributions to the total height at a given actuator position from that actuator and all surrounding actuators. The height of each of the unconstrained actuator displacements is taken as an unknown coefficient in a set of simultaneous equations which are solved on the basis that the total height should be unity at the central actuator and zero at the surrounding actuators. Having determined the unconstrained actuator heights required to give the desired constraint that the net displacement is zero at each of the actuators except for the central one, where it is unity, we use Eq. (3.6) to determine the unit profile at all intervening mesh points.

If the profile is used in the form determined above, no additional adjustments need be made. For convenience, however, we have truncated these profiles along square boundaries. Hence, we slightly adjust the resulting profile to ensure that it satisfies the condition that if all actuators are displaced at unit height, the mirror surface is also at unit height everywhere. The unit profile obtained for a 57-actuator mirror is given in Fig. 3.5. The unit profiles obtained for the 37- and 97-actuators mirrors have the same general characteristics, viz., a monotonic decrease to zero at the nearest neighbor actuators and negative values in the space between these neighboring actuators and the next set of actuators.

The actuator configurations utilized in the simulations are shown in Figs. 3.6, 3.7 and 3.8. Note that extra actuators are placed around the periphery of the mirror. These actuators are used to simulate a mirror having an unconstrained edge. They tend to smooth the transition between the region occupied by the actuators and that which is beyond.

0.	0.	0.	(.0000)	-.0051	-.0050	(.0000)	-.0050	-.0051	(.0000)	0.	0.	0.
0.	0.	-.0079	-.0165	-.0277	-.0390	-.0431	-.0390	-.0277	-.0165	-.0079	0.	0.
0.	-.0079	-.0157	-.0181	-.0269	-.0474	-.0627	-.0474	-.0269	-.0181	-.0157	-.0079	0.
(.0000)	-.0165	-.0181	(.0000)	.0293	.0324	(.0000)	.0324	.0293	(.0000)	-.0181	-.0165	(.0000)
-.0051	-.0277	-.0269	.0293	.1578	.2848	.3334	.2848	.1578	.0293	-.0269	-.0277	-.0051
-.0050	-.0390	-.0474	.0324	.2848	.5859	.7386	.5859	.2848	.0324	-.0474	-.0390	-.0050
(.0000)	-.0431	-.0627	(.0000)	.3334	.7386	(1.0000)	.7386	.3334	(.0000)	-.0627	-.0431	(.0000)
-.0050	-.0390	-.0474	.0324	.2848	.5859	.7386	.5859	.2848	.0324	-.0474	-.0390	-.0050
-.0051	-.0277	-.0269	.0293	.1578	.2848	.3334	.2848	.1578	.0293	-.0269	-.0277	-.0051
(.0000)	-.0165	-.0181	(.0000)	.0293	.0324	(.0000)	.0324	.0293	(.0000)	-.0181	-.0165	(.0000)
0.	-.0079	-.0157	-.0181	-.0269	-.0474	-.0627	-.0474	-.0269	-.0181	-.0157	-.0079	0.
0.	0.	-.0079	-.0165	-.0277	-.0390	-.0431	-.0390	-.0277	-.0165	-.0079	0.	0.
0.	0.	0.	(.0000)	-.0051	-.0050	(.0000)	-.0050	-.0051	(.0000)	0.	0.	0.

Fig. 3.5. Unit profile for a 57-actuator, deformable mirror with nine mesh points per actuator (actuator positions denoted by the brackets).

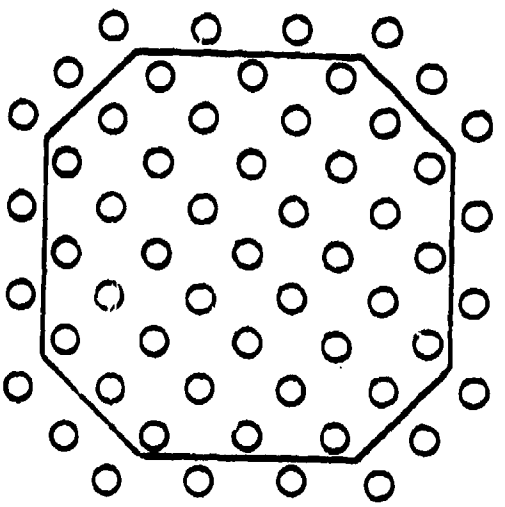

Fig. 3.6. Actuator configuration used in 37-actuator deformable mirror simulation (37 actuators, 20 dummies, 13 mesh points per actuator.

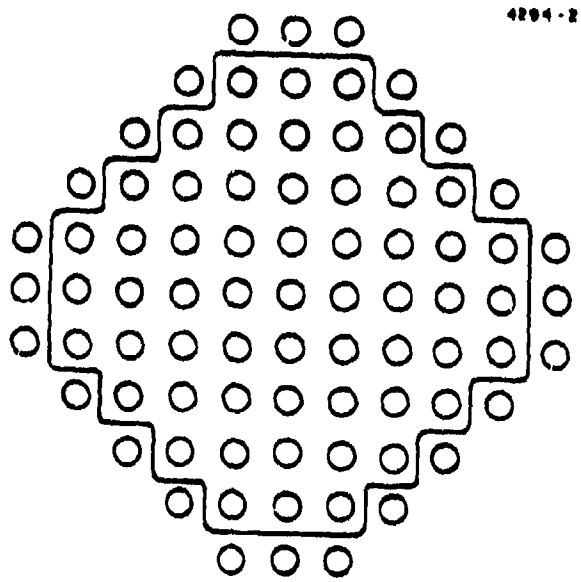

Fig. 3.7. Actuator configuration used in 37-actuator deformable mirror simulation (57 actuators, 24 dummies, 9 mesh points per actuator).

4294-3

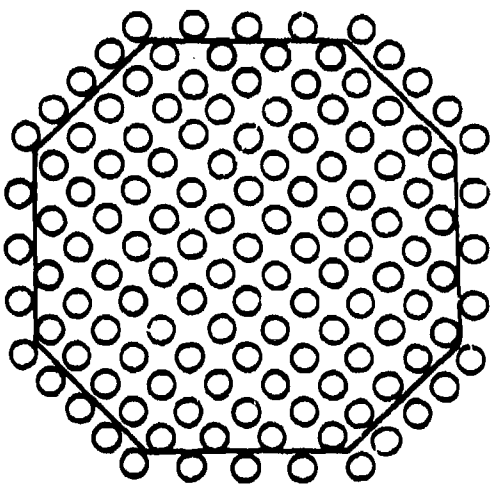

Fig. 3.8. Actuator configuration used in 97-actuator deformable mirror simulation (97 actuators, 32 dummies, 5 mesh points per actuator).

3.4 Propagation Simulation

3.4.1 Formulation — The field of a high-power laser beam propagating through a turbulent atmosphere can be derived from a scalar function $u(\underline{x})$ that satisfies the equation

$$i\,2\,\frac{\partial u}{\partial z} + \nabla_T^2\,u + k^2\left(n^2(\underline{x},t)-1\right)\,u = -\,\frac{\partial^2 u}{\partial z^2} \qquad (3.7)$$

where ∇_T^2 is the transverse Laplacian $\partial^2/\partial x^2 + \partial^2/\partial y^2$, k is the wavenumber $2\pi/\lambda$, and $n(\underline{x},t)$ is the refractive index of the medium. In writing Eq. (3.7), we have assumed that the nominal direction of propagation is along the z axis of an x,y,z coordinate system. At laser wavelengths the function $u(\underline{x},t)$ varies much more rapidly transverse to the direction of propagation than it does along the direction of propagation. This enables us to make the paraxial approximation wherein the term on the right side of Eq. (3.7) is neglected. We then have

$$i\,2k\,\frac{\partial u}{\partial z} + \nabla_T^2\,u + k^2\left(n^2(\underline{x},t)-1\right)\,u = 0 \qquad (3.8)$$

For given initial data, i.e., values of the field at points in the aperture of the laser transmitter (or on the target), the propagation simulator must generate the corresponding field values at the target (or in the receiving aperture) such that Eq. (3.8) is satisfied. To do this, we divide the medium into slabs defined by planes on which z is constant. In going from one slab to the next, we write $u(\underline{x})$ in the form

$$u(\underline{x},t) = \exp\left(\Gamma(\underline{x},t)\right)\,w(\underline{x},t) \qquad (3.9)$$

where $\Gamma(\underline{x},t)$ is a phase function associated with the medium

inhomogeneities between $z-\Delta z/2$ and $z+\Delta z/2$

$$\Gamma(\underline{x},t) = \frac{ik}{2}\int_{z-\Delta z/2}^{z+\Delta z/2} dz'\left(n^2(x,y,z',t)-1\right) \qquad (3.10)$$

The complex amplitude $\omega(\underline{x})$ then satisfies the equation

$$\left[1 + 2ik\frac{\partial}{\partial z} + \exp(-\Gamma)\ \nabla_T^2\ \exp(\Gamma)\right]\omega = 0 \qquad (3.11)$$

with the initial condition

$$\omega(x,y,z,t) = u(x,y,z,t) \qquad (3.12)$$

Physically, these equations approximate the propagation in the inhomogeneous medium by a two-step process at each z increment. First, we propagate the field $u(\underline{x},t)$ at $z-\Delta z/2$ to $z+\Delta z/2$, assuming that the intervening space is homogeneous. The effect of the inhomogeneities between $z-\Delta z/2$ and $z+\Delta z/2$ is then accounted for by multiplying this solution by the phase factor $\exp(\Gamma)$.

3.4.2 Converging Coordinate Transformation — To reduce the size of the mesh required to solve Eq. (3.11) numerically, we use converging coordinates defined by the transformation

$$\xi_1 = \frac{x/r_o}{N(z)} \qquad (3.13)$$

$$\xi_2 = \frac{y/r_o}{N(z)} \qquad (3.14)$$

$$N(z) = \alpha^{-1/2}\left[\left(1-\frac{z}{f}\right)^2 + \alpha^2\left(\frac{z}{k r_o^2}\right)^2\right]^{1/2} \qquad (3.15)$$

$$\xi_3 = \tan^{-1}\left[\frac{(1+\beta)\frac{z}{f}}{\beta^{1/2}} - 1\right] \qquad (3.16)$$

$$\beta^{1/2} = \alpha \frac{f}{k\rho_o^2} \tag{3.17}$$

where ρ_o is a characteristic dimension of the laser beam at the transmitter (e.g., the e-folding radius of a gaussian beam), f is the distance to the focus, and α is a constant determined by the requirement that the solution be confined within the boundaries of the mesh at the focal plane. In the absence of thermal blooming and turbulence, the choice $\alpha = 1$ yields a coordinate system that converges at a rate determined by the free-space diffraction of a gaussian beam having an e-folding radius ρ_o. With turbulence and thermal blooming effects present, we typically choose α in the range 1.5 to 3.0, depending on the amount of additional spreading induced by these effects.

When written in terms of the converging coordinate variables defined above, Eqs. (3.9) and (3.11) for the complex amplitude are replaced by the relations

$$\omega(x,y,z,t) = \hat{\omega}(\underline{\zeta},\xi)\, \exp(\tilde{\Gamma})\, v(\underline{\zeta},\xi,t) \tag{3.18}$$

$$\hat{\omega}(\underline{\zeta},\xi) = \left(\alpha^{1/2}\, N(z)\right)^{-1} \exp\left[\frac{i}{2}\left(\zeta_1^2 + \zeta_2^2\right) \tan\right] \tag{3.19}$$

$$\tilde{\Gamma} = \frac{ik}{2} \int_{z-\Delta z/2}^{z+\Delta z/2} dz' \left(n^2(x,y,z')-1\right) - \frac{i}{2}\left(\zeta_1^2 + \zeta_2^2\right) \Delta\xi \tag{3.20}$$

$$\left[\frac{\partial}{\partial \xi} - \frac{i}{2} \exp(-\tilde{\Gamma}) \left(\frac{\partial^2}{\partial \zeta_1^2} + \frac{\partial^2}{\partial \zeta_2^2}\right) \exp(\tilde{\Gamma})\right] v = 0 \tag{3.21}$$

where $\Delta\xi$ is the increment in ξ in going from $z-\Delta z/2$ to $z+\Delta z/2$. The initial condition for v is

$$v(\underline{\zeta},\xi,t) = \omega(x,y,z,t)/\hat{\omega}(\underline{\zeta},\xi) \tag{3.22}$$

To solve Eq. (3.21) we utilize the fact that for sufficiently small values of $\Delta\xi$ (i.e., Δz) the effect of the exponential factors $\exp(\pm\tilde{\Gamma})$ in this equation is small. Hence, we solve the simpler equation obtained when these factors are equated to unity

$$\left[\frac{\partial}{\partial\xi} - \frac{i}{2}\left(\frac{\partial^2}{\partial\zeta_1^2} + \frac{\partial^2}{\partial\zeta_2^2}\right)\right] v = 0 \qquad (3.23)$$

3.4.3 Method of Solution — We use a fast Fourier transform technique to solve Eq. (3.23). The basis of this approach is the fact that the solution of Eq. (3.23) can be expressed in the form of a discrete Fourier series

$$v(\zeta,\xi,t) = \sum_{m=0}^{N-1}\sum_{n=0}^{N-1} V_{mn}(\xi,t)\,\exp\left[i(p_m\zeta_1+q_n\zeta_2)\right] \qquad (3.24)$$

where the Fourier coefficients V_{mn} are determined from the initial data and Eq. (3.23) as follows. The initial values of V_{mn} are obtained by taking the discrete Fourier transform of the initial values of $v(\zeta,\xi_i,t)$ over a mesh of points $\zeta_1 = [\ell-(N/2)]\,\Delta\zeta$, $\zeta_2 = [j-(N/2)]\,\Delta\zeta$ $(\ell,j = 0,1,\ldots,N-1)$

$$V_{mn}(\xi_i,t) = \frac{(-1)^{m+n}}{N^2}\sum_{\ell=0}^{N-1}\sum_{j=0}^{N-1} v\left(\left(\ell-\frac{N}{2}\right)\Delta\zeta,\left(j-\frac{N}{2}\right)\Delta\zeta,\xi_i,t\right)$$

$$\exp\left[-\frac{i2\pi}{N}(m\ell+nj)\right] \qquad (3.25)$$

The ξ dependence of V_{mn} is then determined by substituting Eq. (3.24) in Eq. (3.23), which yields

$$\frac{\partial V_{mn}}{\partial \xi} + \frac{i}{2}\left(p_m^2 + q_n^2\right) V_{mn} = 0 \qquad (3.26)$$

from which it follows that

$$V_{mn}(\xi,t) = V_{mn}(\xi_i,t)\ \exp\left[-\frac{i\left(p_m^2 + q_n^2\right)\Delta\xi}{2}\right] \qquad (3.27)$$

Finally, it can be shown that in order for the discrete Fourier series representation of v given in Eq. (3.24) to be real when v is real, the coefficients p_m and q_n must have the form

$$p_m = \frac{2\pi}{N\Delta\zeta}\left(m - \frac{N}{2}\right) \qquad (3.28)$$

$$q_n = \frac{2\pi}{N\Delta\zeta}\left(n - \frac{N}{2}\right) \qquad (3.29)$$

Hence, for discrete points $\zeta_1 = (\ell - N/2)\Delta\zeta$, $\zeta_2 = (j - N/2)\Delta\zeta$ $(\ell, j = 0,1,\ldots,N-1)$

$$v\left(\left(\ell - \frac{N}{2}\right)\Delta\zeta,\ \left(j - \frac{N}{2}\right)\Delta\zeta,\ \xi\ ,\ t\right)$$

$$= (-1)^{\ell+j} \sum_{m=0}^{N-1} \sum_{n=0}^{N-1} (-1)^{m+n}\ V_{mn}(\xi_i,t)$$

$$\exp\left[-\ i\ \hat{\beta}\left(\left(\frac{m - \frac{N}{2}}{N}\right)^2 + \left(\frac{n - \frac{N}{2}}{N}\right)^2\right) + i\ \frac{2\pi}{N}\ (\ell m + jn)\right] \qquad (3.30$$

where $\hat{\beta} = 2\pi^2\Delta\xi/(\Delta\zeta)^2$. Note that v is simply $(-1)^{\ell+j}$ times the discrete Fourier transform of $(-1)^{m+n}\ V_{mn}(\xi,t)$.

The effect of the medium and the factor $\exp[(-i/2(\zeta_1^2 + \zeta_2^2)\Delta\xi]$ introduced by the coordinate transformation is taken into account at each ξ step in the calculation by multiplying the value of v obtained in the previous step by the quantity $\exp(\tilde{\Gamma})$ defined in Eq. (3.20), i.e., the initial value inserted in Eq. (3.25) is $\exp(\tilde{\Gamma})$ times the value of v determined from the previous steps.

3.4.4 Effect of Absorption — The absorptive contribution to $\tilde{\Gamma}$ is calculated from the relations

$$\tilde{\Gamma}_{abs}(x,y,z,t) = \frac{ik\gamma_o}{2} \int_{z-\Delta z/2}^{z+\Delta z/2} dz' \left(\frac{\Delta\rho}{\rho_o}\right)_{abs} \tag{3.31}$$

$$\left(\frac{\Delta\rho}{\rho_o}\right)_{abs} = \frac{(\gamma-1)\ \alpha\ \exp(-\alpha_T z)\ E_{pulse}}{\gamma\ P_o\ \pi\ a^2\ N^2(z)} \sum_{m=0}^{M-1} |v(\zeta_1-\zeta_{1m},\zeta_2,\xi,mt_p)|^2 \tag{3.32}$$

with

$$\zeta_{1m} = \frac{(M - m)\ (v_o + \Omega z)\ t_p}{N(z)\ a} \tag{3.33}$$

where γ is the ratio of the specific heat of air at constant pressure to that at constant volume ($\gamma = 1.4$), α is the molecular absorption coefficient of the air, α_T is the total extinction coefficient, v_o is the transverse wind velocity assumed to be in the x direction, P_o is the ambient air pressure, Ω is the slew rate (slewing assumed also to be in the x direction), E_{pulse} is the energy per pulse, and γ_o is the molecular polarizability of air.

In writing Eq. (3.32) we have assumed that the laser energy is delivered in a series of pulses for which the pulse length is short enough that no heating occurs during a pulse.

Moreover, we have assumed that the interval between pulses is long enough that the heating caused by the m^{th} pulse is fully developed by the time that the $m + 1^{st}$ pulse arrives (i.e., transient density changes traveling at the velocity of sound are assumed to have departed from the region occupied by the beam).

3.4.5 Effect of Turbulence — The contribution to $\tilde{\Gamma}$ from turbulence is calculated by a Fourier transform technique which yields a two-dimensional distribution of gaussian random numbers having correlation properties consistent with those associated with the phase variations caused by Kolmogorov turbulence. In particulare, we represent $\tilde{\Gamma}_{turb}$ by the Fourier-Stieltjes integral

$$\tilde{\Gamma}_{turb}(\underline{x}) = i \int d\tilde{\Gamma}(\underline{K}) \exp(i\, \underline{K} \cdot \underline{x}) \tag{3.34}$$

The increments $d\tilde{\Gamma}$ satisfy the relations

$$\langle d\tilde{\Gamma}(\underline{K}) \rangle = 0 \tag{3.35}$$

$$\langle d\tilde{\Gamma}(\underline{K}_1)\, d\tilde{\Gamma}^*(\underline{K}_2) \rangle = 0 \qquad \underline{K}_1 \neq \underline{K}_2$$

$$= d\underline{K}_1\, \Phi_{\tilde{\Gamma}}(\underline{K}_1) \qquad \underline{K}_1 = \underline{K}_2 \tag{3.36}$$

where $\Phi_{\tilde{\Gamma}}(\underline{K})$ is the spatial spectrum of the phase variations and $\underline{K}$ is the spatial wavenumber. Note that, with this representation, $\tilde{\Gamma}_{turb}$ satisfies the Weiner-Khintchin theorem

$$\left\langle \tilde{\Gamma}_{turb}(\underline{x}_1)\, \tilde{\Gamma}^*_{turb}(\underline{x}_2) \right\rangle = \int d\underline{K}\, \Phi_{\tilde{\Gamma}}(\underline{K}) \exp\left[i\, \underline{K} \cdot (\underline{x}_1 - \underline{x}_2) \right] \tag{3.37}$$

as required by any valid representation of a homogeneous random process.

We have utilized a modified von Karman spectrum for $\Phi_{\tilde{\Gamma}}$

$$\Phi_{\tilde{\Gamma}}(\underline{K}) = \frac{.207\ C_N^2\ k^2\ \Delta z\ K_o^{-11/3}}{\left(1 + \frac{K^2}{K_o^2}\right)^{11/6}} \tag{3.38}$$

where C_N^2 is the index structure constant, Δz is the z increment, and K_o is 2π divided by the outer scale of turbulence L_o. The Fourier integral in Eq. (3.34) is evaluated by the following discrete Fourier transform approximation of this integral

$$\tilde{\Gamma}_{turb}(m,n)$$

$$= i(-1)^{m+n} \sum_{\ell=0}^{N-1} \sum_{j=0}^{N-1} \frac{(-1)^{\ell+j}\ a_{\ell j}\ \exp\left[i\ \frac{2\pi}{N}\ (m\ell + nj)\right]}{\left[1 + \left(\left(\ell - \frac{N}{2}\right)^2 + \left(j - \frac{N}{2}\right)^2\right)\left(\frac{L_o}{N\Delta x}\right)^2\right]^{11/12}} \tag{3.39}$$

where the $a_{\ell j}$ are complex gaussian random numbers (we assume that $\tilde{\Gamma}_{turb}$ is gaussian) with zero mean and the following correction properties

$$a^*_{\ell j} = a_{N-\ell, N-j} \tag{3.40}$$

$$\left\langle \text{Real}(a_{\ell j})\ \text{Imag}(a_{\ell' j'}) \right\rangle = 0 \qquad \text{all } \ell, j \tag{3.41}$$

$$\left\langle \text{Real}(a_{\ell j})\ \text{Real}(a_{\ell' j'}) \right\rangle = 0 \qquad \ell' \neq \ell, j' \neq j \text{ and } \ell' \neq N-\ell, j' \neq N-j \tag{3.42}$$

$$\left\langle \text{Imag}(a_{\ell j})\ \text{Imag}(a_{\ell' j'}) \right\rangle = 0 \qquad \ell' \neq \ell, j' \neq j \text{ and } \ell' \neq N-\ell, j' \neq N-j \tag{3.43}$$

$$\left\langle \text{Real}(a_{\ell j})\ \text{Real}(a_{\ell' j'}) \right\rangle = 1 \qquad \ell' = \ell, j' = j \text{ or } \ell' = N-\ell, j' = N-j \tag{3.44}$$

$$\left\langle \text{Imag}(a_{\ell j})\ \text{Imag}(a_{\ell' j'}) \right\rangle = 1 \qquad \ell' = \ell, j' = j \tag{3.45}$$

$$\left\langle \text{Imag}(a_{\ell j})\ \text{Imag}(a_{\ell' j'}) \right\rangle = -1 \qquad \ell' = N-\ell, j' = N-j \tag{3.46}$$

The quantity σ is the constant

$$\sigma = .070\left(k^2\ C_N^2\ \Delta z\ L_o^{5/3}\right)^{1/2}\ \frac{L_o}{N\Delta x} \tag{3.47}$$

where Δx is the distance between mesh points.

Evidence that the random phase screens, generated in the manner described above, have the desired statistical properties is provided by the phase structure function results shown in Fig. 3.9. The theoretical value for the phase structure function for the spectrum Φ_Γ given in Eq. (3.38) is

$$D_\phi(r) = \left\langle \left(\phi(\underline{x}_1) - \phi(\underline{x}_2)\right)^2 \right\rangle$$

$$= 2.61\ k^2\ C_N^2\ \Delta z\ K_o^{-5/3} \left[.6 - \frac{(K_o\ r/2)^{5/6}\ K_{5/6}(K_o\ r)}{\Gamma(11/16)} \right] \tag{3.48}$$

$$r = |\underline{x}_1 - \underline{x}_2| \tag{3.49}$$

which in the limit of an infinite outer scale reduces to

$$D_\phi(r) = 2.91\ k^2\ C_N^2\ \Delta z\ r^{5/3} \qquad L_o \to \infty \qquad (3.50)$$

The dashed curved line and the straight line in Fig. 3.9 are phase structure function results calculated from Eqs. (3.48) and (3.50). The somewhat wiggly solid line is the phase structure function result obtained by averaging over 100 realizations of phase screen samples generated by a fast Fourier transform evaluation of the relation given in Eq. (3.39). In these runs we used a 64 x 64 mesh with 1.106 cm between mesh points and an outer scale length of two meters.

3.4.6 Medium Storage and Update — At each ξ step in the propagation calculation we store the absorptive contribution to Γ (although this is done in large core memory on the CDC 7600 computer that we are using, it could also be done by writing on the disk). The effect of a transverse wind and of slewing is taken into account in this storage process by first performing a mesh translation on the new and old data. The data are moved a distance equal to the distance that the wind and slewing moves the heated air between pulses. Hence, the stored values of Γ_{abs} are those that will be seen by the next pulse.

Rather than calculate Γ_{turb} anew for each pulse in a multipulse sequence, we calculate a single set of phase screens at the outset and store them for later use. The effect of the wind and slewing is taken into account by translating these phase screens as described above.

The overall logic and sequence of events in the propagation simulation, including the medium storage and update processes described above, are indicated in the flow diagram given in Fig. 3.10.

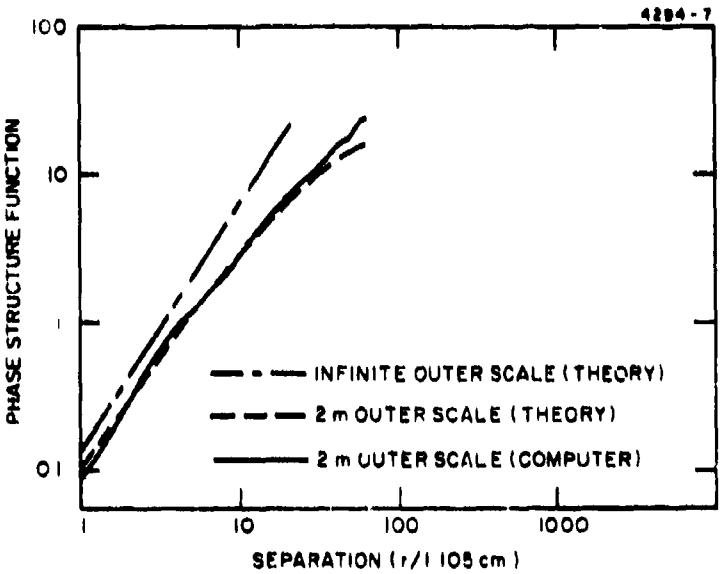

Fig. 3.9. Comparison of computer calculated and theoretical phase structure function results.

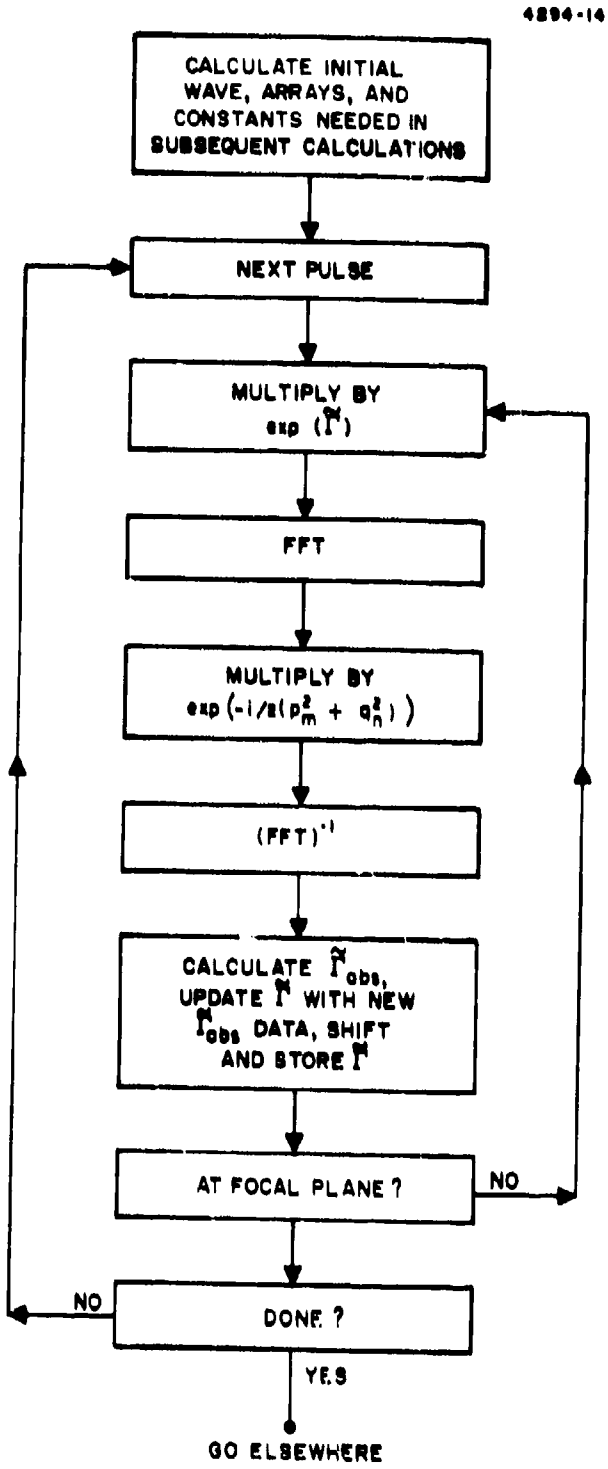

Fig. 3.10. Flow diagram for propagation simulator.

3.5 Target Simulation

The essence of the closed-loop adaptive optical control concept is that the reflection characteristics of typical targets are such that highlights or glints will exist and that the return from these regions can be used as a reference to sense the changes in the transmitter phase distribution required to correct for atmospheric phase distortions. Hence, we approximate the target by a set of glints. Each glint is represented as a gaussian reflectivity distribution, i.e.,

$$\text{Reflectivity Distribution} = \sum_{m=1}^{M} \rho_m(\underline{x}) \qquad (3.51)$$

$$\rho_m(\underline{x}) = a_m \exp\left[-\frac{(x - \underline{x}_m)^2}{\bar{x}_m^2}\right] \qquad (3.52)$$

where m is the number of glints and a_m, $\underline{x}_m$, $\bar{x}_m$ are the strength, position and width of the m^{th} glint.

The initial data for the return wave are determined by multiplying the incident laser field by the target reflectivity function given in Eq. (3.51).

IV. SIMULATION RESULTS

4.1 Mirror Simulation Results

The major portion of the effort on the mirror simulation has been devoted to the problem of determining the number of mirror actuators required to yield a good fit to the phase surfaces that must be generated to compensate for the effects of atmospheric turbulence. In addition to the computer simulation results, we have obtained analytical estimates of the effects of turbulence on peak irradiance at a target, both with and without adaptive compensation. The analytical results obtained for the effect of turbulence on peak irradiance without adaptive compensation are discussed in Section 4.1.1. Analytical and computer simulation results obtained from the effect of adaptive compensation with a mirror having a finite number of degrees of freedom (i.e., actuators) are discussed in Section 4.1.2.

We also have done some work on the dependence of mirror fit on the number of mirror actuators for the case of phase conjugate compensation for the effects of thermal blooming. These results are discussed in Section 4.1.3.

4.1.1 Effect of Turbulence on Peak Irradiance — An interpretation of theoretical results derived for the ensemble-averaged irradiance distribution of a laser beam propagated through atmospheric turbulence[5] indicates that the effect of the turbulence can be accounted for by introducing an appropriately chosen random phase screen in front of the transmitter aperture. Utilizing this result, we can write the Strehl ratio (SR) associated with the turbulence in the form (recall that the Strehl ratio due to a wave distortion is defined as the ratio of the peak irradiance in the presence of the distortion to the peak irradiance of the undistorted beam)

$$SR = \frac{\langle I(0) \rangle}{\langle I(0) \rangle_{\text{no turb}}} = \frac{\int d\underline{x}' \int d\underline{x}'' \; u_o(\underline{x}') \; u_o^*(\underline{x}'') \; \exp\left[-\frac{1}{2} D_\phi(\underline{x}'-\underline{x}'')\right]}{\int d\underline{x}' \int d\underline{x}'' \; u_o(\underline{x}') \; u_o(\underline{x}'')} \qquad (4.1)$$

where u_o is the aperture field distribution and $D_\phi(\underline{x}'-\underline{x}'')$ is the phase structure function of the random phase screen. For Kolmogorov turbulence with an infinite outer scale, the appropriate phase structure function is

$$D_\phi(\underline{x}'-\underline{x}'') = 2.91 \; k^2 \; |\underline{x}'-\underline{x}''|^{5/3} \int_o^z dz' \left(\frac{z'}{z}\right)^{5/3} C_N^2(z') \qquad (4.2)$$

where C_N^2 is the index structure constant, k is the wavenumber $2\pi/\lambda$ and z is the distance to the target.

For a uniformly illuminated circular aperture of diameter d, the Strehl ratio obtained from Eq. (4.1) is

$$SR = \frac{16}{\pi} \int_o^1 d\zeta \; \zeta \left[\cos^{-1}(\zeta) - \zeta(1-\zeta^2)^{1/2}\right] \exp\left(-\beta \; \zeta^{5/3}\right) \qquad (4.3)$$

with

$$\beta = 1.456 \; k^2 \; d^{5/3} \int_o^z dz' \left(\frac{z'}{z}\right)^{5/3} C_N^2(\underline{z}') \qquad (4.4)$$

$$= 3.44 \left(\frac{d}{r_o}\right)^{5/3} \qquad (4.5)$$

where r_o is the phase coherence length defined by Fried

$$6.88 \; r_o^{-5/3} = 2.91 \; k^2 \int_o^z dz' \left(\frac{z'}{z}\right)^{5/3} C_N^2(z') \qquad (4.6)$$

Numerical results for the Strehl ratio defined in Eq. (4.3) are shown in Fig. 4.1 (curve labeled "no adaptive optics") for values of β up to 15. For larger values of β, the following asymptotic result applies

$$SR \sim 4.407 \; \beta^{-6/5} - 5.692 \; \beta^{-9/5}, \quad \beta \geq 15 \qquad (4.7)$$

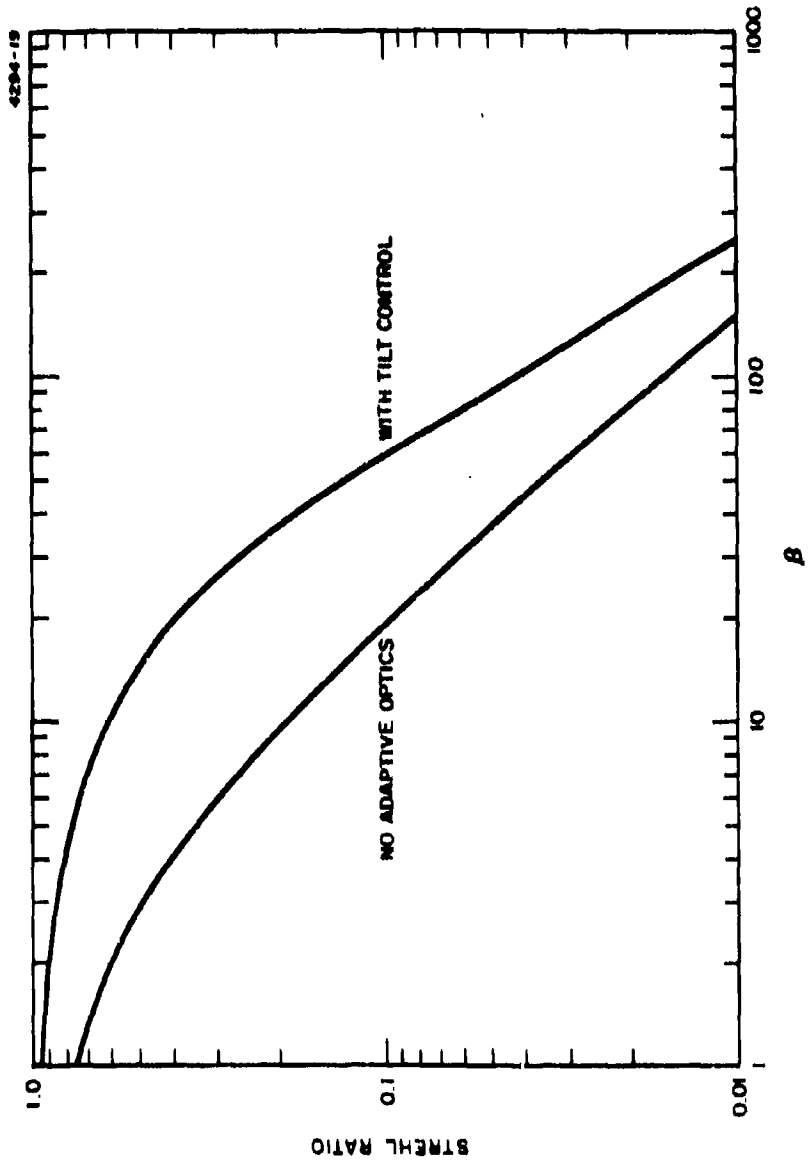

Fig. 4.1. Strehl ratio due to Kolmogorov turbulence.

Note that for sufficiently large β, the Strehl ratio is given by the first term in Eq. (4.7) and from Eq. (4.5) this can be written simply as the ratio $(r_o/d)^2$, which is inversely related to the number of phase coherence areas contained in the transmitter aperture.

The effect of having an adaptive tilt control system that dynamically removes the tilt component of the turbulence distortion can be accounted for by replacing the structure function D_ϕ in Eq. (4.1) by $D_\phi - \langle(\underline{a} \cdot (\underline{x}'-\underline{x}''))^2\rangle$ where $\underline{a}$ is a least squares estimate of the instantaneous tilt vector. Utilizing the results for $\underline{a}$ derived by Fried,[6] we can write the following expression for the Strehl ratio obtained for a uniformly illuminated circular aperture having adaptive tilt control

$$(SR)_{\substack{\text{with tilt}\\ \text{control}}} = \frac{16}{\pi} \int_o^1 d\zeta\, \zeta \cos^{-1}\left[\zeta - \zeta(1-\zeta^2)^{1/2}\right] \exp\left[-\beta\, \zeta^{5/3}\, (1-\zeta^{1/3})\right] \qquad (4.8)$$

Numerical results for the Strehl ratio defined in Eq. (4.8) are shown in Fig. 4.1 (curve labeled "with tilt control"). To assist in the use of Fig. 4.1 we have plotted β as a function of $C_N^2\, z$ in Fig. 4.2. It appears that tilt control alone is a reasonably effective compensation technique for values of β less than 20. At 10.6 μm this condition will be satisfied in many scenarios, whereas at 3.8 μm it will seldom be satisfied (e.g., we note from Fig. 4.2 that β is less than 20 for .7 m optics at 10.6 μm for all values of $C_N^2\, z < 2 \times 10^{-10}$ $m^{1/3}$ which, for a 4 km path, requires that $C_N^2 < 2.5 \times 10^{-15}$ $cm^{-2/3}$).

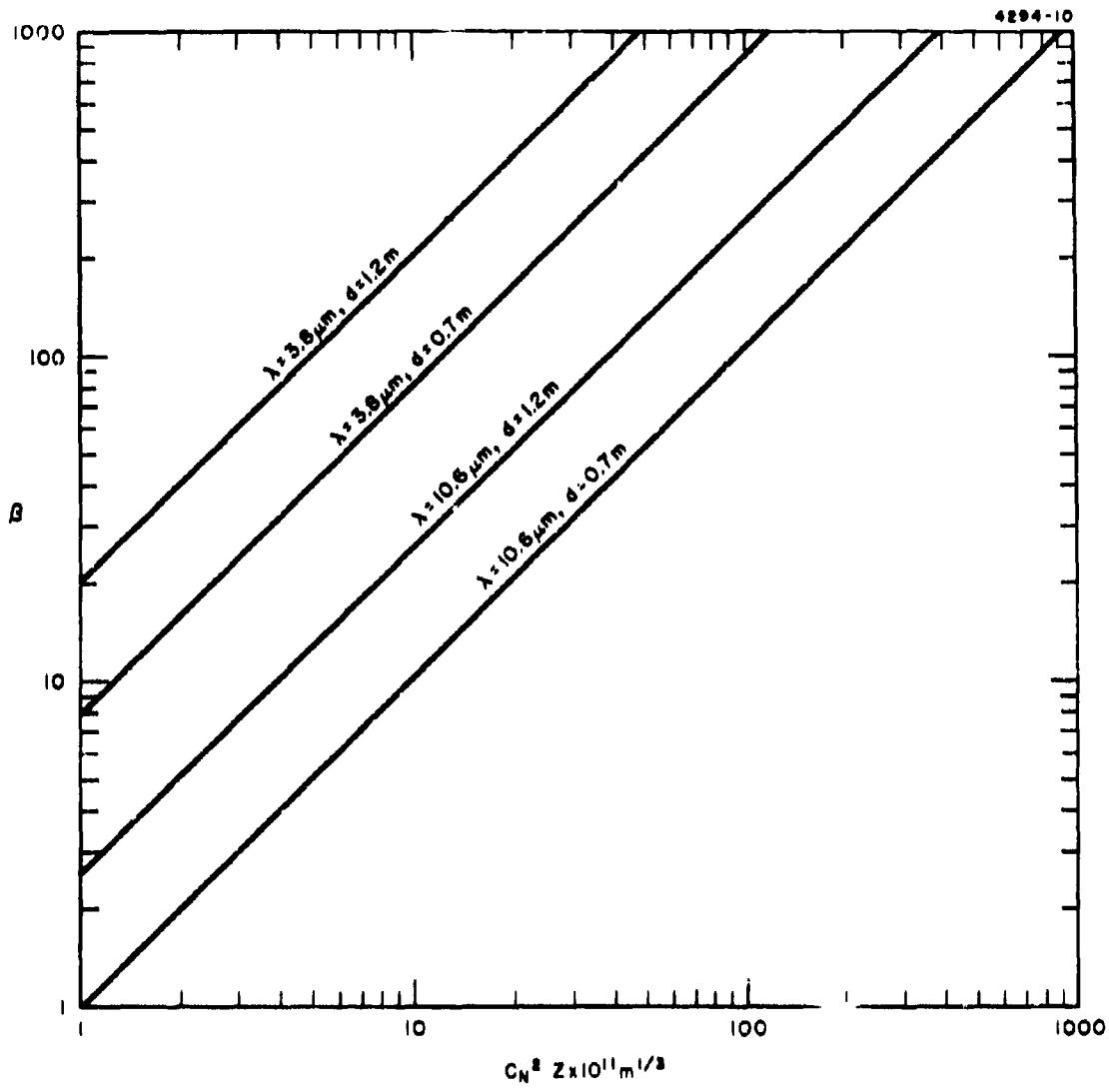

Fig. 4.2. β versus C_N^2 for homogeneous turbulence.

4.1.2 Adaptive Compensation for Turbulence Effects — Effect of Having a Finite Number of Actuators — It was noted in the previous section that the effect of atmospheric turbulence on the ensemble-averaged irradiance distribution can be accounted for by introducing a random phase screen in front of the transmitting aperture. The appropriate phase distribution is that which would be produced by a point source located on the target.* This implies that an ideal adaptive optics system should be able to completely compensate for the effects of the turbulence by introducing the conjugate phase distribution as a correction.† The degree to which this is achieved depends on whether the target has a point-glint scatterer that provides the requisite phase information and on the degree to which the adaptive optics system can reproduce the desired phase distribution. In this section we shall assume that the target has a point-glint scatterer so that the ability of the adaptive optics system to compensate for the turbulence depends solely on its ability to reproduce the desired phase distribution. This depends largely on the number of degrees of freedom possessed by the correcting optics.

To a good approximation, we can represent the finite spatial bandwidth of the optics by writing the residual phase error, i.e., the difference between the desired phase distribution and the actual distribution obtained from the optics, in the form

---

*In this discussion, and in that given in Section 4.1.1, we assume that amplitude scintillation effects are small. If they are not small, the effect of atmospheric turbulence cannot be represented simply by a phase screen but rather we must also introduce a random apodization.

†Subject to the assumption that amplitude effects are negligible.

$$\Delta\phi(\underline{x}) = \phi(\underline{x}) - \frac{\int d\underline{x}'\, h(\underline{x} - \underline{x}')\, \phi(\underline{x}')}{\int d\underline{x}'\, h(\underline{x}')} \tag{4.9}$$

with

$$h(\underline{x}) = 1, \quad |\underline{x}| < b$$

$$= 0, \quad |\underline{x}| > b \tag{4.10}$$

In this representation the effect of the finite spatial bandwidth of the optics is approximated by a spatial averaging process, i.e., we assume that the phase correction introduced by the adaptive optics at a point is a uniformly weighted average of the desired phase correction at all surrounding points within a circle of radius b. For deformable optics, we can relate the value of b to the number of mirror actuators N_a by noting that the spatial spectrum of the weighting function $h(\underline{x})$ is $[2J_1(Kb)/Kb]^2$, which has appreciable magnitude only in the domain $Kb \lesssim 3$. More precisely, we have found that good agreement is obtained between the theory discussed here and the mirror simulation results discussed later if $Kb = 2.72$ where K is the cutoff wavenumber of the mirror. (Note that the spectrum of the weighting function h is less than .1 for all $Kb \geq 2.72$.) Hence, since the Nyquist frequency of a mirror having actuators separated by a distance γ_a is π/γ_a, we let

$$b = \frac{2.72}{\pi}\,\gamma_a = \frac{2.72}{\pi}\left(\frac{\pi}{4N_a}\right)^{1/2} d \tag{4.11}$$

where d is the mirror diameter.

The Strehl ratio obtained in the presence of the residual phase error $\Delta\phi$ defined in Eq. (4.9) is given by Eq. (4.1) with the structure function D replaced by

$$D_{\Delta\phi}(\underline{x}' - \underline{x}'') = \left\langle \left(\Delta\phi(\underline{x}') - \Delta\phi(\underline{x}'') \right)^2 \right\rangle \qquad (4.12)$$

which in the case of Kolmogorov turbulence with an infinite outer scale can be written

$$D_{\Delta\phi}(\underline{x}' - \underline{x}'') = 6.454 \left(\frac{u}{r_o} \right)^{5/3} \int_o^\infty d\zeta \; \zeta^{-8/3} \left[1 - J_o(\zeta) \right] \left[\frac{1 - 2J_1\left(\frac{b}{u} \zeta \right)}{\frac{b}{u} \zeta} \right]^2 \qquad (4.13)$$

with $u = |\underline{x}' - \underline{x}''|$ and r_o given by Eq. (4.2). For a uniformly illuminated circular aperture of diameter d, the corresponding expression for the Strehl ratio obtained with adaptive correction is

$$SR = \frac{16}{\pi} \int_o^1 d\zeta \; \zeta \left[\cos^{-1} \zeta - \zeta (1-\zeta^2)^{1/2} \right] \exp\left[-\beta \, \zeta^{5/3} \, f\left(\zeta, \frac{b}{d} \right) \right] \qquad (4.14)$$

with β given by Eq. (4.5) and

$$f\left(\zeta, \frac{b}{d} \right) = \frac{\int_o^\infty d\xi \; \xi^{-8/3} \left[1 - J_o(\xi) \right] \left[1 - \frac{2J_1\left(\frac{b}{d} \xi \right)}{\frac{b}{d} \xi} \right]^2}{\int_o^\infty d\xi \; \xi^{-8/3} \left[1 - J_o(\xi) \right]} \qquad (4.15)$$

We have evaluated the integral in Eq. (4.14) numerically and have found that, over a wide range of values for the parameters β and b/d, it is approximated extremely well by the result obtained when $f(\zeta, b/d)$ is replaced by its asymptotic result for $b/d\zeta \gg 1$, which is

$$f\left(\frac{b}{d}\right) = .145\left(\frac{b}{d}\right)^{5/3} \qquad \frac{b}{d} \leq 1 \tag{4.16}$$

The corresponding expression for the SR is

$$SR \approx \exp\left(-.145\ \beta\left(\frac{b}{d}\right)^{5/3}\right)$$

$$= \exp\left(-.093\ \beta\ N_a^{-5/6}\right) \tag{4.17}$$

where we have used the relation between b/d and N_a given in Eq. (4.11). The discrepancy between the approximation in Eq. (4.17) and the more exact result in Eq. (4.14) is significant only for very large values of β and small values of N_a. This is illustrated by Fig. 4.3 which shows the results obtained for $\beta = 35.41$ and 177.05. For values of N_a greater than 5 the discrepancy is less than one percent.

To provide a check on the above analytical work, we have performed two types of mirror simulations. In each, the effect of a turbulent phase screen placed in front of an aperture was compensated by a mirror with a finite number of actuators. The average Strehl ratio obtained from a sequence of five independent phase screens was determined as a function of the number of actuators. In one of the simulations the deformable mirror software described in Section 3.3 was used in conjunction with a sinusoidal multidither COAT algorithm of the type used previously at HRL in our COAT servo system studies.[2] In the other simulation the mirror was modeled by a segmented mirror with piston and tilt control on each segment. The piston and tilt settings for each segment were determined by a least squares fit to the random phase surface over the segment. The results obtained from these simulations are summarized in Fig. 4.4. The agreement between the piston and tilt results and the theoretical predictions obtained from

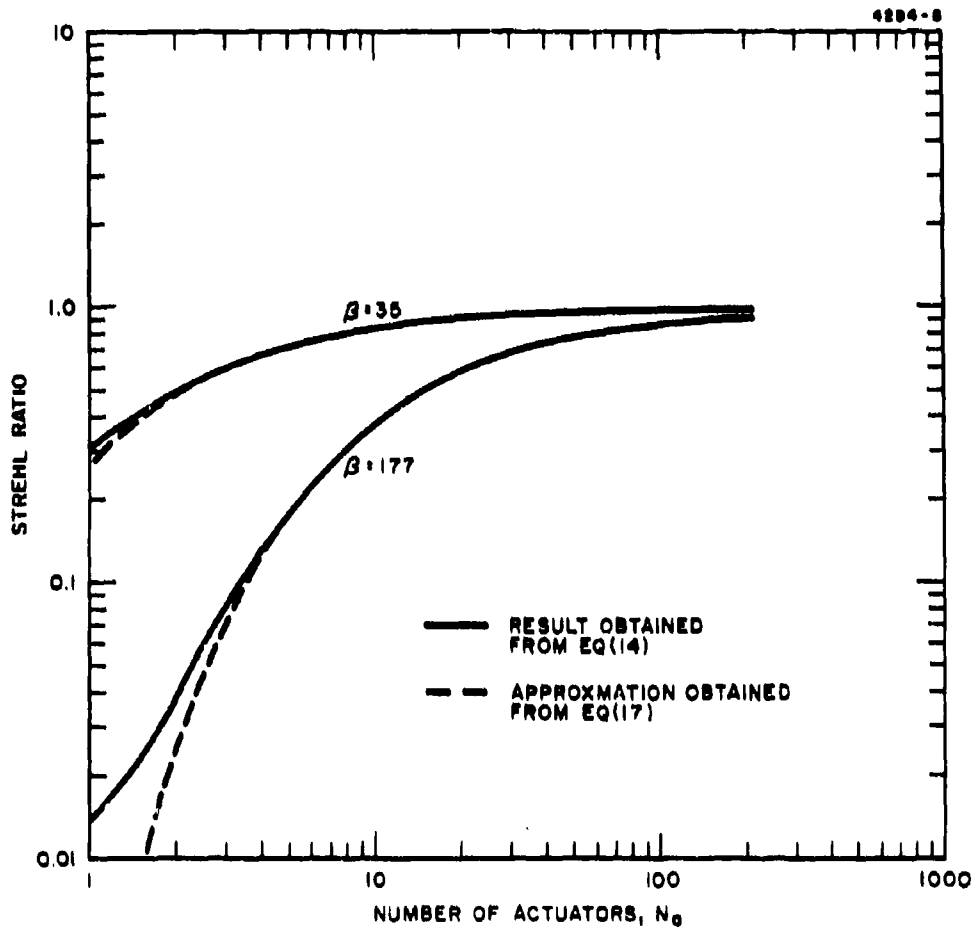

Fig. 4.3. Comparison of Strehl ratio estimates.

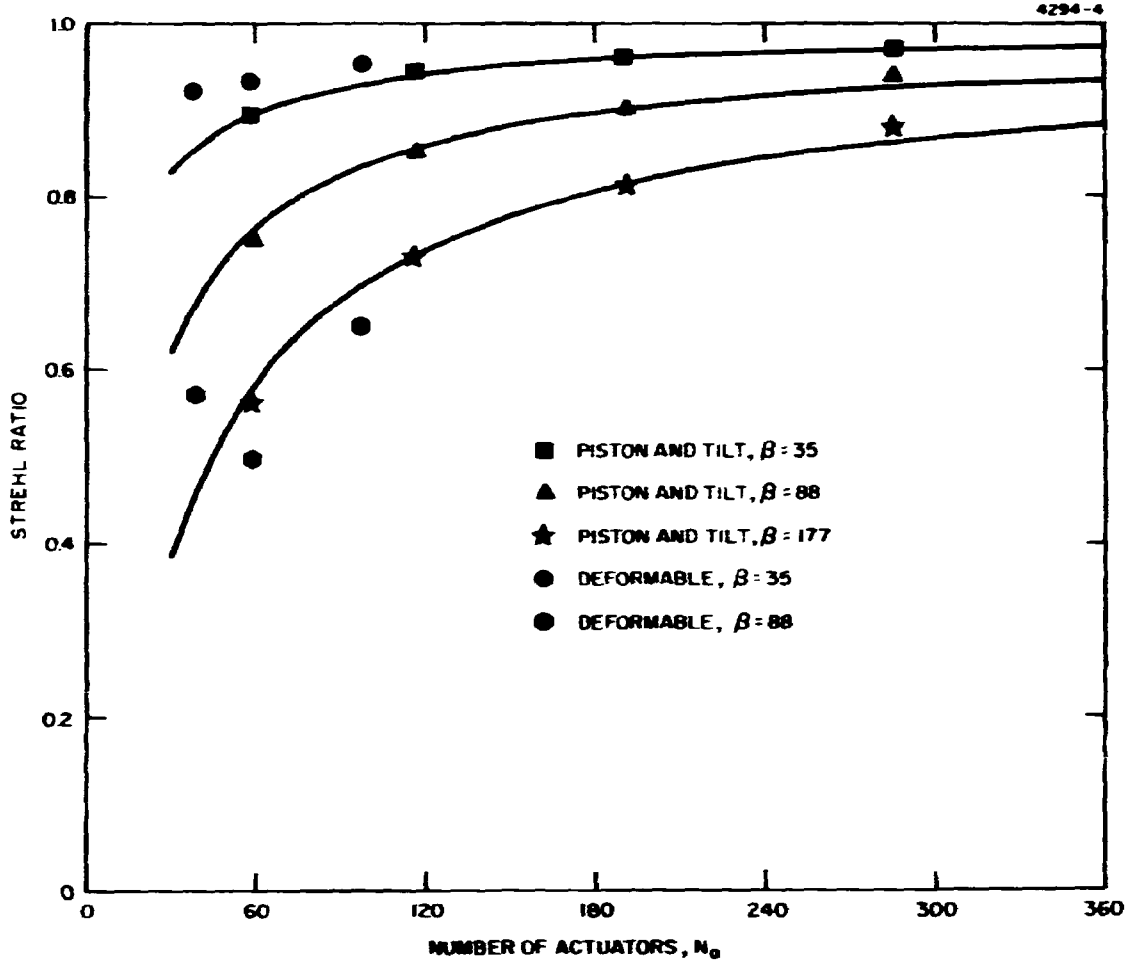

Fig. 4.4. Comparison of numerical and analytical Strehl ratio results (piston and tilt data obtained from a least squares fit routine, deformable mirror data obtained with a sinusoidal multidither control algorithm.

Eqs. (4.14) and (4.17) is very good for all values of β, which gives us confidence in the theoretical results given in these equations. We believe that these results are representative of those that would be obtained with a deformable mirror in the absence of the $2N\pi$ problem discussed below. The results actually obtained with a deformable mirror will depend on the degree to which the $2N\pi$ problem is avoided.

The agreement between the theory and the deformable mirror-multidither COAT simulation results is reasonably good for moderate values of β but is poor for large values of β. We attribute the poor results obtained at large values of β to a $2N\pi$-type of behavior. The deformable mirror simulation that was used in these runs has a $2N\pi$ correction loop that introduces a 2π correction whenever the phase difference between actuators exceeds four radians. The intent is to suppress 2π errors introduced by the servo system. However, if the phase distortion that is to be removed by the mirror changes by more than four radians between actuators, the 2π "correction" introduced by the $2N\pi$ correction loop is, in fact, a 2π error and the mirror performance is corresponding degraded. This problem could be avoided by removing the $2N\pi$ correction loop but then we would be faced with $2N\pi$ servo errors. One way to avoid this problem is to use more actuators so that the phase change between actuators never exceeds four radians. Another way would be to design the mirror so that the likelihood of $2N\pi$ errors is reduced, in which case the $2N\pi$ correction loop could be eliminated. More work clearly needs to be done on this problem.

4.1.3 Compensation for Thermal Blooming Phase Profiles — As a part of our effort to provide an understanding of the reasons for the relatively meager improvement in beam quality realized with phase conjugate compensation, we have investigated the nature of the phase distribution of the return wave in the thermal blooming problem. We have found

that the phase of the return wave reflected from a gaussian glint in the target plane does not vary nearly as much as one would expect based on the type of calculation performed by Lincoln Laboratory in their optimization studies.[2]

Specifically, the phase correction used in the Lincoln Laboratory work is of the form

$$\Delta\phi = \frac{\hat{\gamma}}{2} \frac{N_D}{N_\omega} \ln(1 + N_\omega) \int_{-\infty}^{\zeta_1} d\zeta_1' \, |u(\zeta_1', \zeta_2, 0)|^2 \qquad (4.18)$$

where N_D and N_ω are the distortion and slewing numbers which, in the notation used in this report, are given by the relations

$$N_D = \frac{\gamma_o(\gamma-1)\,\alpha\, P\, kf}{\gamma\, v_o\, P_o\, \pi\, \rho_o} \qquad (4.19)$$

$$N_\omega = \Omega f / v_o \qquad (4.20)$$

γ_o is the polarizability of the air, γ is the ratio of the specific heats at constant pressure and volume, α is the absorption coefficient, P is the average power, k is the wavenumber, f is the focal distance, v_o is the crosswind velocity, P_o is the ambient atmospheric pressure, ρ_o is the e-folding radius of the laser beam (which we assume to have a gaussian irradiance distribution), and Ω is the slew rate. The factor $\hat{\gamma}$ is a constant that the Lincoln Laboratory work indicates is nearly equal to 1.5 for good phase compensation under a variety of initial beam conditions.

For a gaussian beam truncated outside a circle of diameter $3\rho_o$, the maximum phase excursion predicted by Eq. (4.18) is

Max. Phase Excursion $= \Delta\phi(\infty) - \Delta\phi(-\infty)$

$$= \frac{\hat{\gamma}}{2} \frac{N_D}{N_\omega} \ln(1+N_\omega) \int_{-1.5}^{1.5} d\zeta' \exp(-\zeta'^2)$$

$$= \frac{.856\ \hat{\gamma}\ N_D}{N_\omega} \ln(1+N_\omega) \qquad (4.21)$$

and if $\hat{\gamma} = 1.5$, $N_D = 21.6$, and $N_\omega = 4$, this predicts a maximum phase excursion of 11.2 radians. In comparison, we have measured a maximum phase excursion for the field reflected from a gaussian glint under equivalent conditions (for N_D and N_ω) to be only about two radians. We believe that this discrepancy is caused principally by the extended nature of the target glint, i.e., it is a gaussian glint rather than a point glints, and that this discrepancy supports our contention that the disappointingly small amount of correction achieved with phase conjugate compensation is related to the isoplanatic problem discussed in Section 2.1.

4.2 Phase Compensation for the Effects of Turbulence and Thermal Blooming

As mentioned earlier, we have obtained phase compensation data only for the case in which a phase conjugate control policy is used. Since all return wave adaptive optical systems use the conjugate phase as a correction (see the discussion in Section 2.1), the data that we have obtained apply to all such systems; e.g., they apply to conventional phase conjugate systems, to return-wave multidither systems, and to all systems based on a maximization of the sharpness of an image of the target.

All of the data were obtained with the time-dependent propagation code described in Section 3.4. Since we were

primarily interested in the correction obtainable under cw conditions, we attempted to choose pulse repetition frequencies that yield good approximations to the cw blooming condition. The pulse repetition frequency required to yield conditions comparable to those existing with cw propagation depends on the beam diameter, distance to the focus, wind velocity, and slew rate. Generally, it is necessary to choose a repetition rate high enough that an air parcel moves only a fraction of the diffraction-limited beam diameter between pulses. This condition can be expressed in the form

$$\text{Pulse Repetition Frequency} \gg \frac{v_o\left(1 + \frac{\Omega f}{v_o}\right)}{\frac{f}{k\rho_o}} \qquad (4.22)$$

where v_o is the transverse wind velocity, Ω is the slew rate, f is the focal distance, k is the wavenumber and ρ_o is a characteristic beam dimension of the transmitted beam (e.g., the e-folding radius of a gaussian beam).

Figure 4.5 shows a comparison of results obtained with the time-dependent code and a cw code. In this case we plot the Strehl ratio (peak irradiance in the presence of distortion divided by the peak irradiance obtainable without distortion) of an untruncated gaussian beam focussed at 2 km. Other parameter values applicable to these results are an average power level of 50 kW, a wavelength of 10.6 μm, an e-folding radius ρ_o of 23 cm (90% of the energy of the initial gaussian beam contained with a 70 cm diameter circle), an absorption coefficient of 2×10^{-6} cm^{-1}, a crosswind velocity v_o of 10 m/sec, and a slew rate Ω equal to zero. Apparently, a pulse repetition frequency of 1000 Hz or more is required to simulate cw propagation under these conditions. This result is in good agreement with the condition given in Eq. (4.22), which predicts that v_{rep} must exceed 682 Hz. As an aside, it is interesting to note the reduction in the distorting effect of thermal blooming at the lower repetition frequencies.

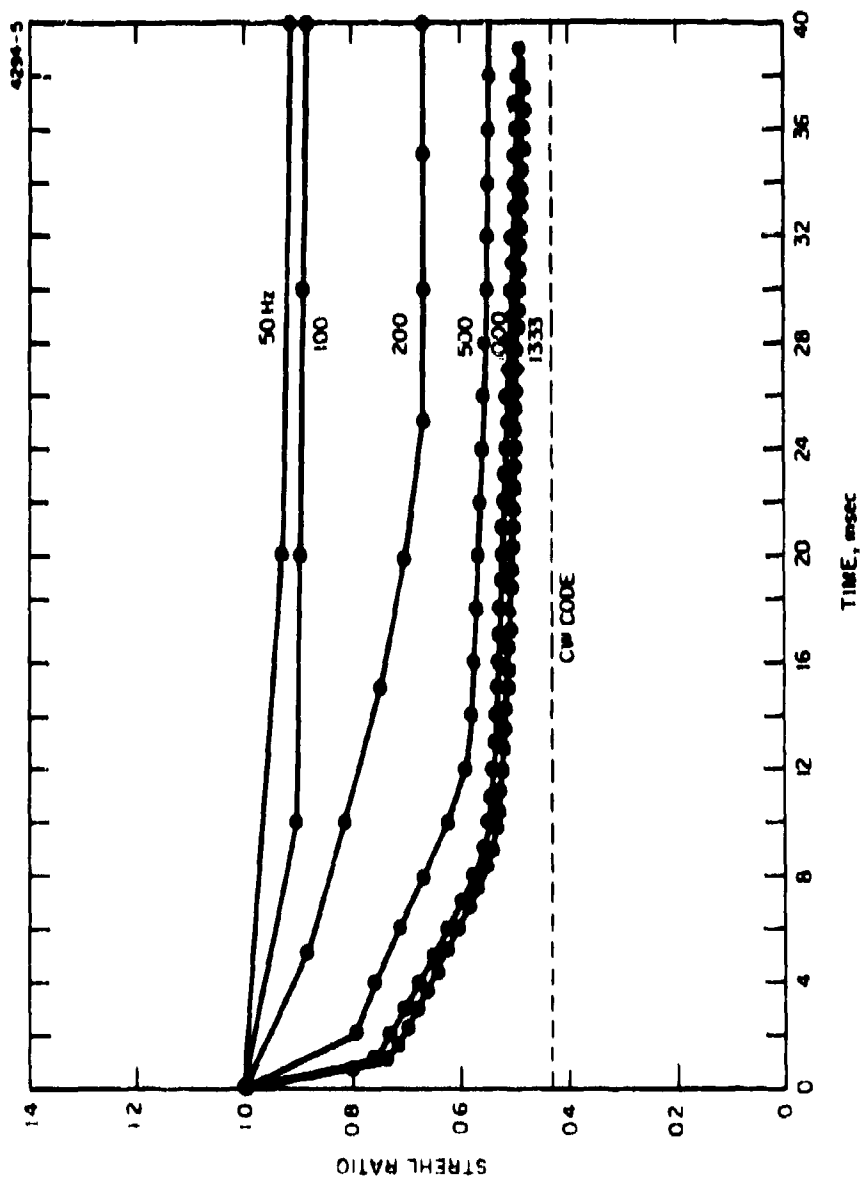

Fig. 4.5. Strehl ratio versus pulse repetition frequency and time.

It becomes increasingly more expensive to simulate cw conditions as the slew rate increases. The reason for this can be seen from the data in Fig. 4.5. Note that the number of pulses required to reach a steady state, be it the cw state or not, tends to increase linearly with increasing pulse repetition frequency. But increasing slew rates imply increasing pulse repetition frequencies, as indicated in Eq. (4.22). Hence, we must propagate more pulses to reach a steady state as Ω increases. In our calculations we have used the largest pulse repetition frequency consistent with the dual requirements that we simulate the cw state and yet do not require an excessive number of pulses. Typically, we have used no more than 20 pulses for a given simulation. At high slew rates, this has resulted in some departure of the multipulse of results from those that would be obtained from a cw code. Principally, the difference is that for a given average power the multipulse results tend to yield Strehl ratios that are 30 to 40% higher than those obtained from a cw code. The same type of power optimization curves are obtained except that the peak irradiance and the transmitter power required to yield the peak are higher (see Fig. 4.6 for example). This discrepancy between the multipulse and cw results is not important in our studies because the main goal of these studies is to ascertain the efficacy of adaptive optics as a technique for increasing the magnitude of the peak irradiance at the target, not to establish the precise power level at which that peak occurs.

In order to determine the relative amount of correction to be expected for turbulence and thermal blooming effects, we have made runs in which one or the other of these effects was absent. In addition, we have obtained data for adaptive compensation of the combined effects of turbulence and thermal blooming. In all of these calculations we have used a phase conjugate correction algorithm in which the transmitter

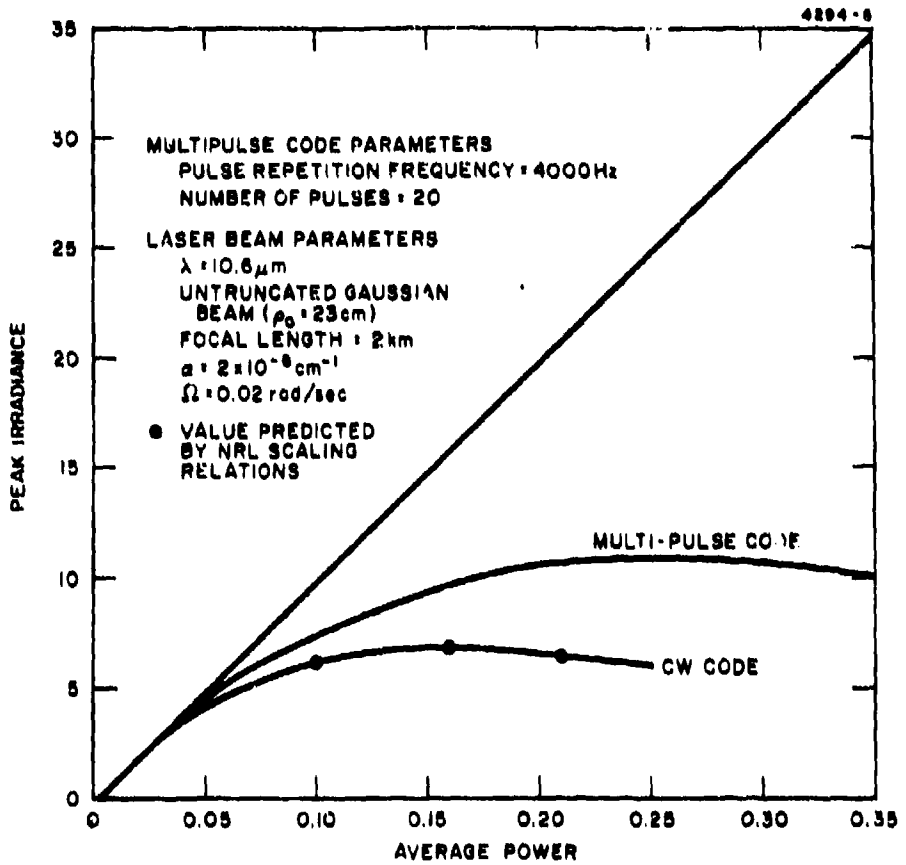

Fig. 4.6. Comparison of power optimization curves obtained from the multipulse and cw propagation codes.

phase was equated on a mesh-point-by-mesh-point basis to the negative of the phase returned from the target. The target was represented by a single gaussian glint having an e-folding width equal to 4 cm. The results obtained for propagation at a CO_2 laser wavelength of 10.6 μm are discussed in Section 4.2.1 and those obtained for propagation at a DF laser wavelength of 3.8 μm are discussed in Section 4.2.2. In these calculations the absorption coefficient was assumed equal to 2×10^{-6} cm^{-1} at 10.6 μm and 4×10^{-7} cm^{-1} at 3.8 μm.

4.2.1 Phase Conjugate Compensation at 10.6 μm — One of the more interesting results from these studies is the observation that much better thermal blooming compensation is obtained with untruncated gaussian beams than with truncated gaussian beams. An example of the results obtained with an untruncated gaussian beam is shown in Fig. 4.7, which applies to the propagation of a beam having an e-folding radius of 23 cm (90% of the energy in the initial irradiance distribution is contained within a circle having a 70 cm diameter), a slew rate of 20 mrad/sec, a focal distance of 2 km, and an index structure constant $C_N^2 = 0$ (i.e., no turbulence). Phase conjugate compensation increases the peak irradiance by a factor of 2.3 and the transmitter power at which the peak occurs is increased by a factor of two. For comparison, the results obtained for a gaussian beam truncated at a beam radius of 35 cm, with all other beam and scenario parameters identical to those discussed above, are shown in Fig. 4.8. In this case, phase conjugate compensation increases the peak irradiance only by about 30%. We believe that the difference in phase compensation achieved with and without beam truncation can be explained by the isoplanatic problem discussed in Section 2.1. As shown in Fig. 4.9, the fields within the circle of beam truncation returned from points within the domain of an extended glint, such as the gaussian glint used in our numerical studies, pass through air that

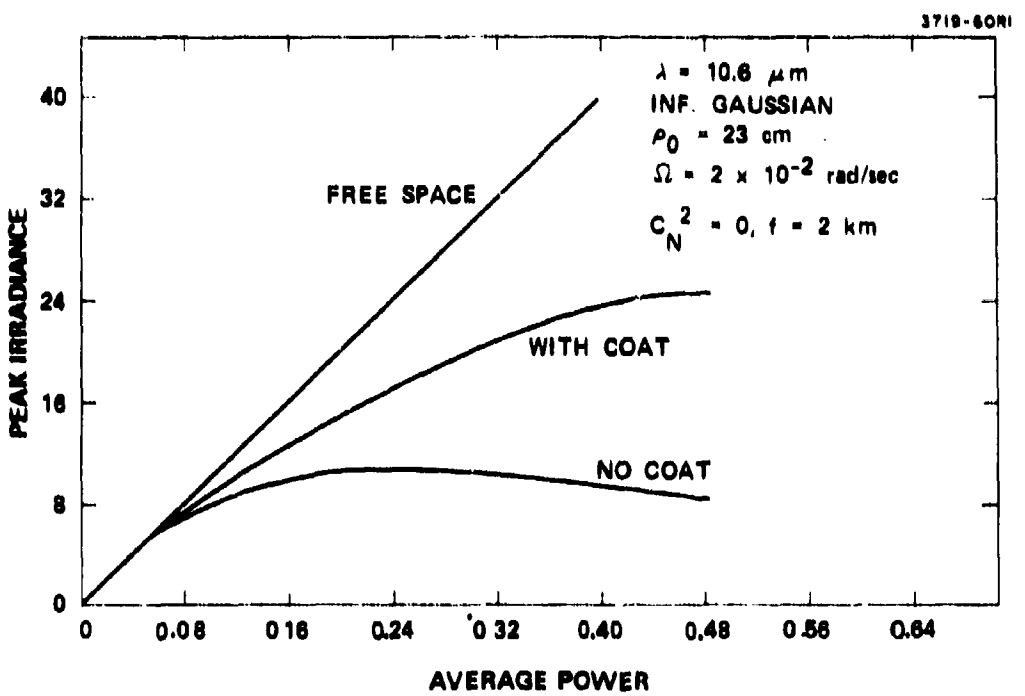

Fig. 4.7. Phase conjugate correction of an infinite gaussian beam.

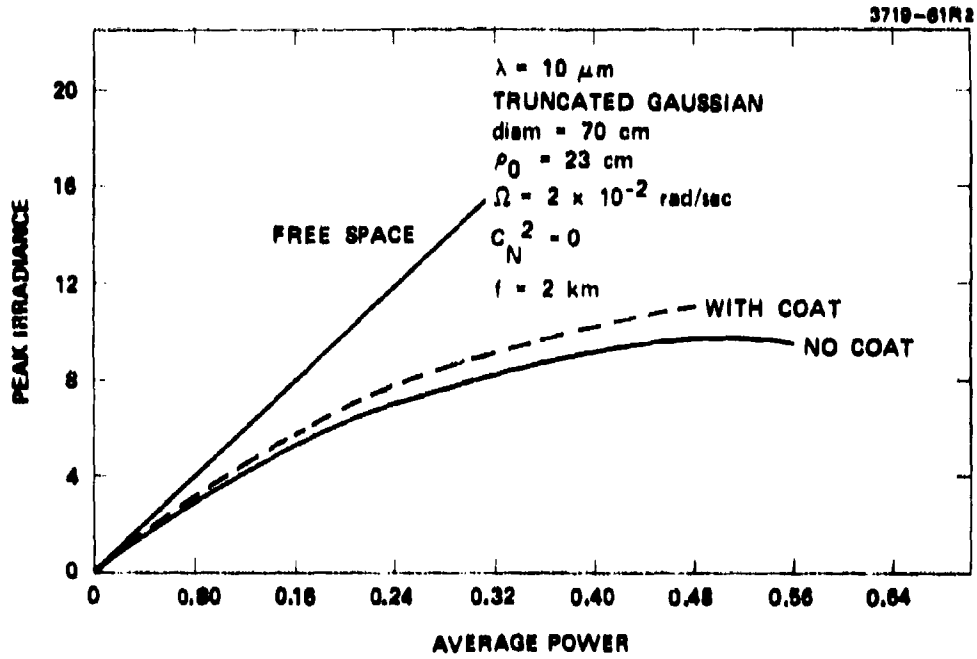

Fig. 4.8. Phase conjugate compensation of a truncated gaussian beam.

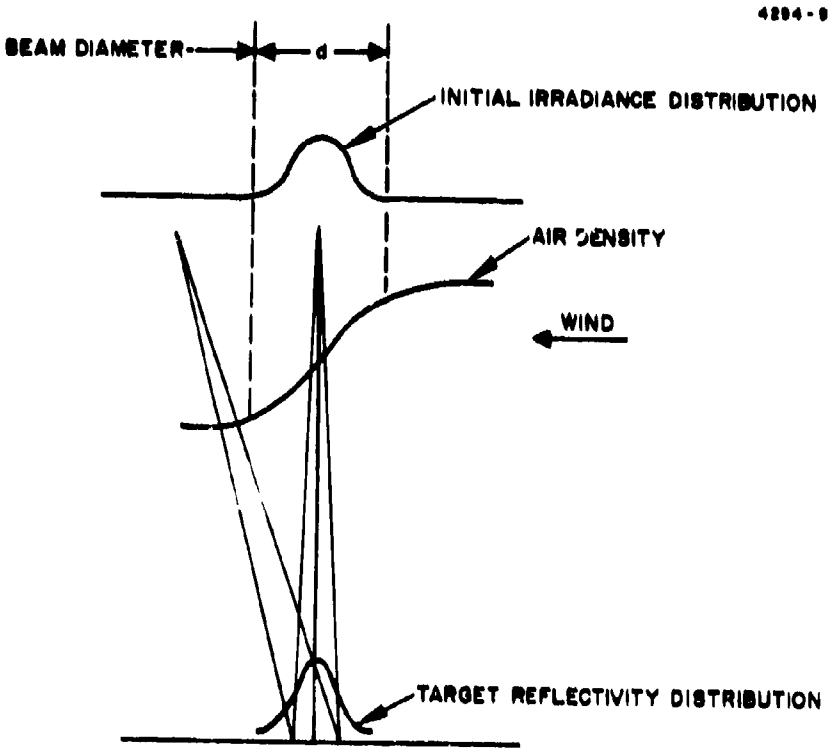

Fig. 4.9. Isoplanatic problem.

has much larger density gradients than the fields returned outside of the circle of beam truncation. Hence, the distorting effect that a finite glint has on the phase of the return wave is less severe outside of the region of truncation than it is within this region and, therefore, better compensation should be obtained with infinite beams than with truncated. In fact, it appears that for the infinite beam case shown in Fig. 4.7 almost all of the factor of 2.3 increase in target irradiance is obtained from fields outside of a 70 cm diameter circle.

Results for phase conjugate compensation of the combined effects of turbulence and thermal blooming are shown in Figs. 4.10, 4.11 and 4.12. All of these results apply to truncated gaussian beams propagated through a single realization of a random medium; i.e., no ensemble-averaging over different random medium realizations was done. Generally, these results, and others that we have obtained, indicate that phase conjugate compensation yields good compensation for the effects of turbulence but very little for the effects of thermal blooming. Fortunately, the ability to compensate for the effects of turbulence is apparently not degraded by the presence of thermal blooming effects even though phase conjugate compensation is not very effective as a thermal blooming compensation technique. The net improvement in beam quality obtained with phase conjugate compensation is most impressive for the conditions depicted in Fig. 4.12 which applies to a 1.2 m beam propagated through moderately streng turbulence having an index structure constant of 6×10^{-15} $cm^{-2/3}$. This is to be expected, of course, since turbulence effects are most pronounced in the case of large beams and high turbulence levels.

The severity of the thermal blooming problem for cw propagation at 10.6 μm has engendered a considerable amount of interest recently in multipulse propagation in which the time between pulses is sufficient to allow the local cross-wind velocity to convect partially the heated air from the

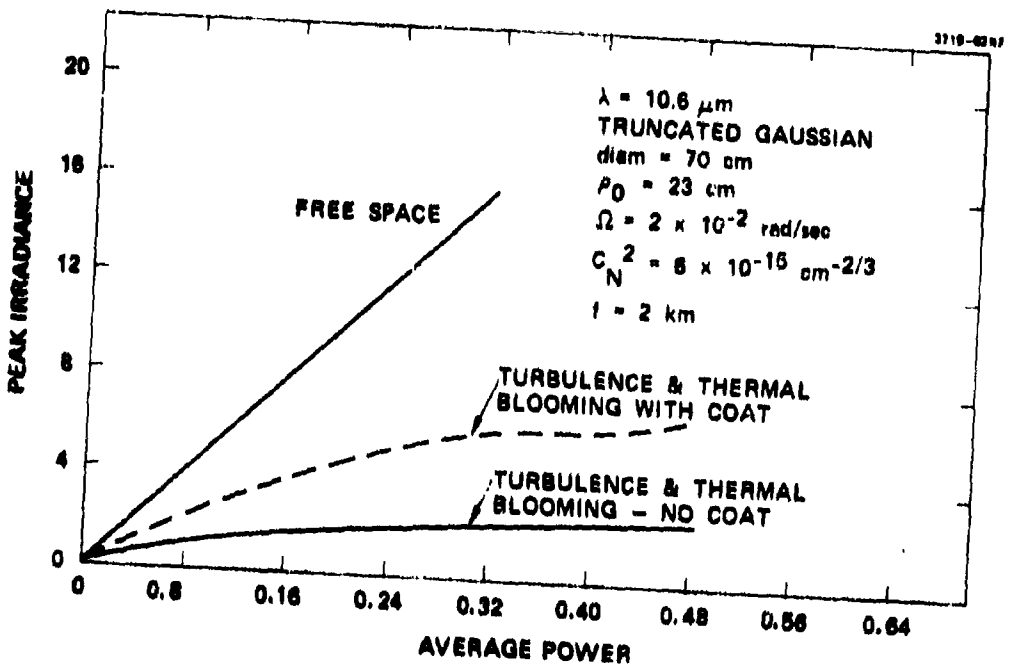

Fig. 4.10. Phase conjugate compensation for the combined effects of turbulence and thermal blooming.

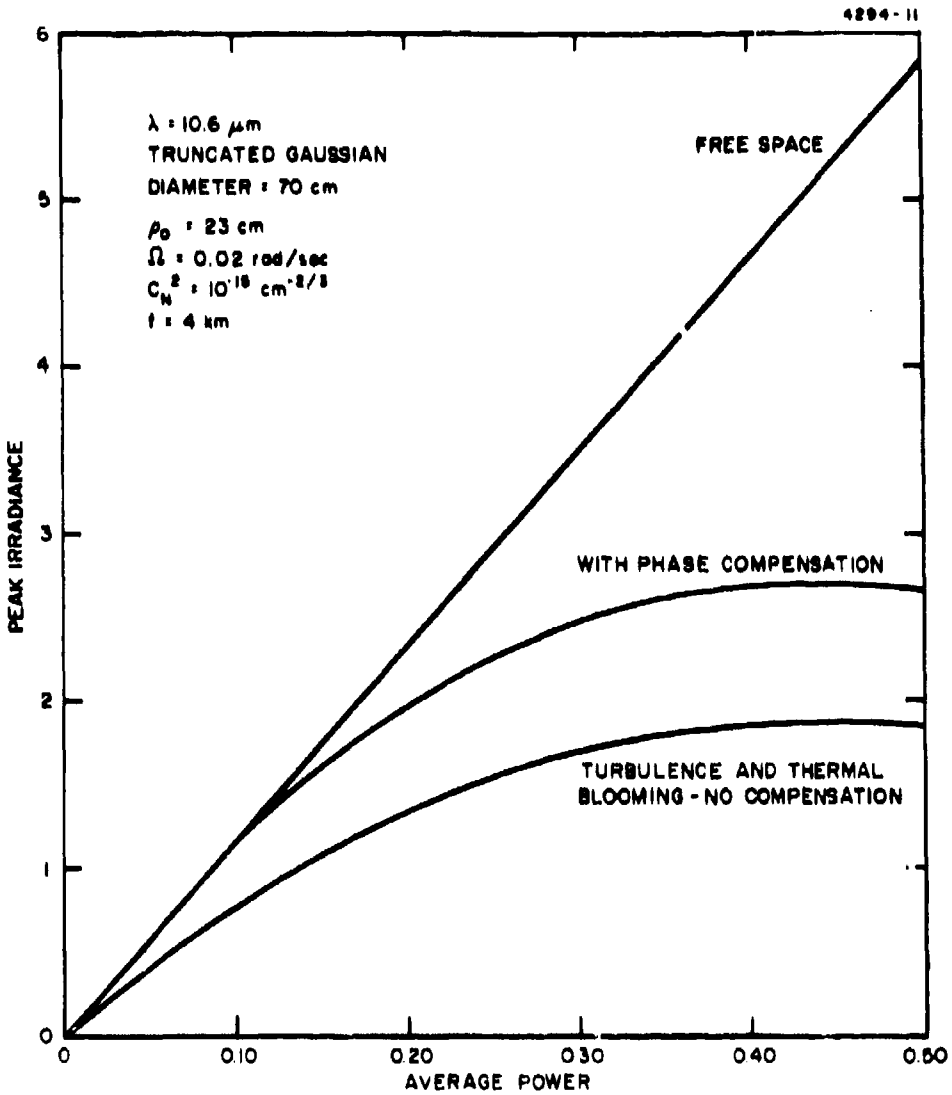

Fig. 4.11. Phase conjugate compensation for the combined effects of turbulence and thermal blooming.

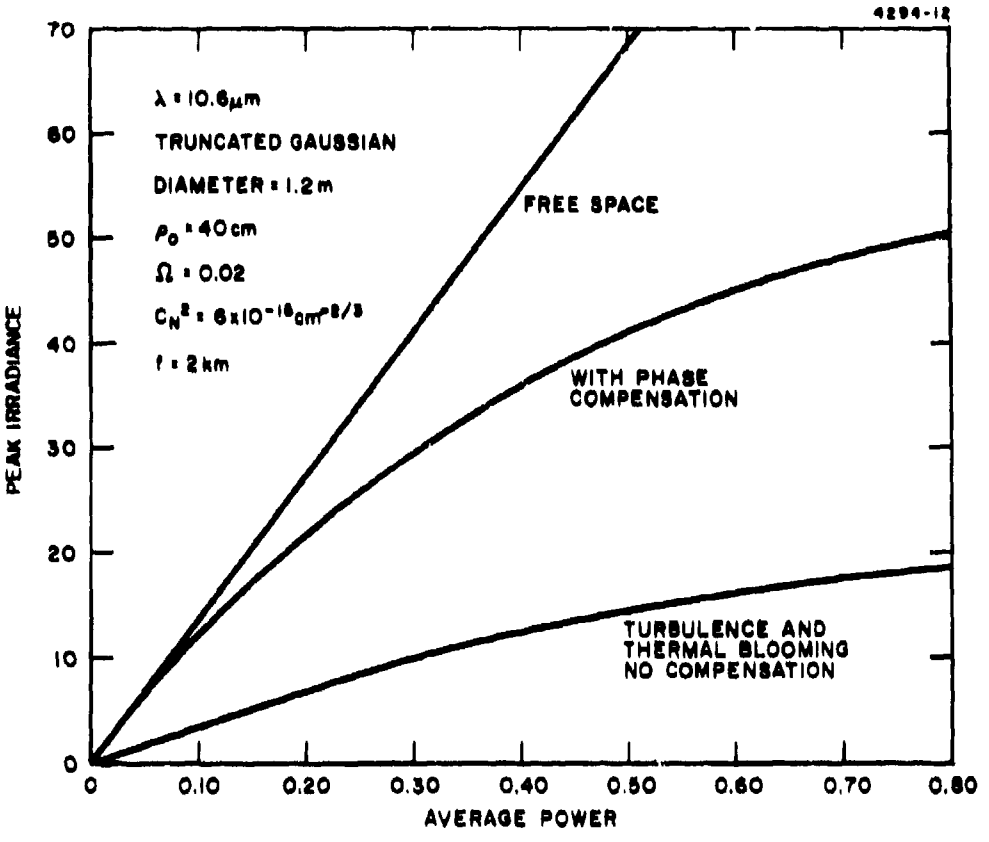

Fig. 4.12. Phase conjugate compensation for the combined effects of turbulence and thermal blooming.

region occupied by the beam. This is a favorable situation for thermal blooming compensation because the blooming under these conditions tends to occur closer to the transmitter and is, therefore, more nearly a pure phase effect which can be corrected by a compensating phase distribution on the transmitted wave. Moreover, the deleterious effects of the isoplanatic problem discussed in Section 2.1 are greatly alleviated so that we should obtain significantly better phase compensation results in the multipulse mode than we have for cw propagation. This is illustrated by the results shown in Fig. 4.13. These results apply to phase conjugate compensation for the residual effects of thermal blooming on the propagation of 12 kJ pulses of 10.6 μm energy radiated in a truncated gaussian beam having a diameter of 70 cm and an e-folding radius of 23 cm (90% of the energy in the gaussian contained within a circle having a 70 cm diameter). The crosswind velocity is 10 m/sec and the beam is being slewed at 20 mrad/sec. The results are plotted as a function of average power, which is related to the pulse repetition rate ν_{rep} by

$$P_{AV} = \nu_{rep} E_{pulse} \tag{4.23}$$

The effect of thermal blooming within a pulse is neglected in this calculation. This should be relatively small for short pulse lengths. For the conditions pertaining to the results in Fig. 4.13, the minimum pulse length consistent with having a peak irradiance below the sea level air breakdown threshold of 10^7 watts/cm^2 is 10 μsec. (This assumes that the Strehl ratio is not degraded by thermal blooming effects.) The significant increase in target irradiance obtained with phase compensation verifies that multipulse propagation is a very favorable mode of operation for phase compensation.

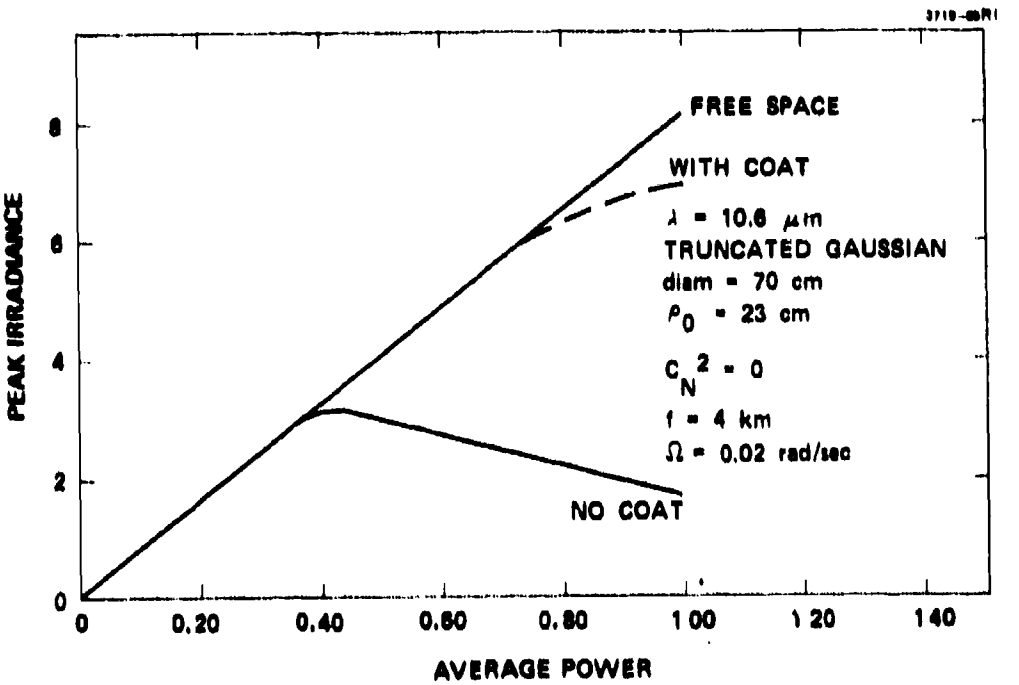

Fig. 4.13. Phase conjugate compensation for multipulse thermal blooming effects at 10.6 μm.

4.2.2 Phase Conjugate Compensation at 3.8 μm — The phase conjugate correction results obtained at 3.8 μm are consistent with those obtained at 10.6 μm in that we have observed that significant correction is achieved for turbulence effects but that very little correction is realized for thermal blooming. The impressive amount of correction achievable for turbulence effects in the absence of thermal blooming is illustrated by the Strehl ratio results given in Figs. 4.14 and 4.15 which apply to a case in which the index structure constant is 10^{-15} $cm^{-2/3}$. The results in Fig. 4.14 pertain to a gaussian beam with an e-folding radius of 13.8 cm (90% of the energy in the initial irradiance distribution is contained within a circle having a 40 cm diameter) truncated outside a 70 cm diameter circle. The path length is 2 km and the slew rate is 20 mrad/sec. The results in Fig. 4.15 apply to a gaussian beam with an e-folding radius of 40 cm (90% of the energy in the initial irradiance distribution is contained within a circle having a 1.2 m diameter) truncated outside a 1.2 m circle. The path length in this case is 4 km and the slew rate is 5 mrad/sec. In both cases the Strehl radio obtained with correction eventually attains a value within 10 to 20% of the free-space value. Although the results in Fig. 4.15 exhibit a rather slow increase in Strehl ratio with successive pulses until the twelfth pulse, we believe that an actual phase conjugate system would increase the Strehl ratio much faster. The slow build-up seen in Fig. 4.15 is probably caused by the fact that we did not iterate the correction process at each step; rather, a single phase measurement was made based on the return of a single reference pulse propagated just prior to the high power pulse. The single pulse reference is adequate when the beam is in a nearly converged state, as it is later on in the pulse train, but does not give an accurate phase estimate early in the pulse sequence. Early in the pulse

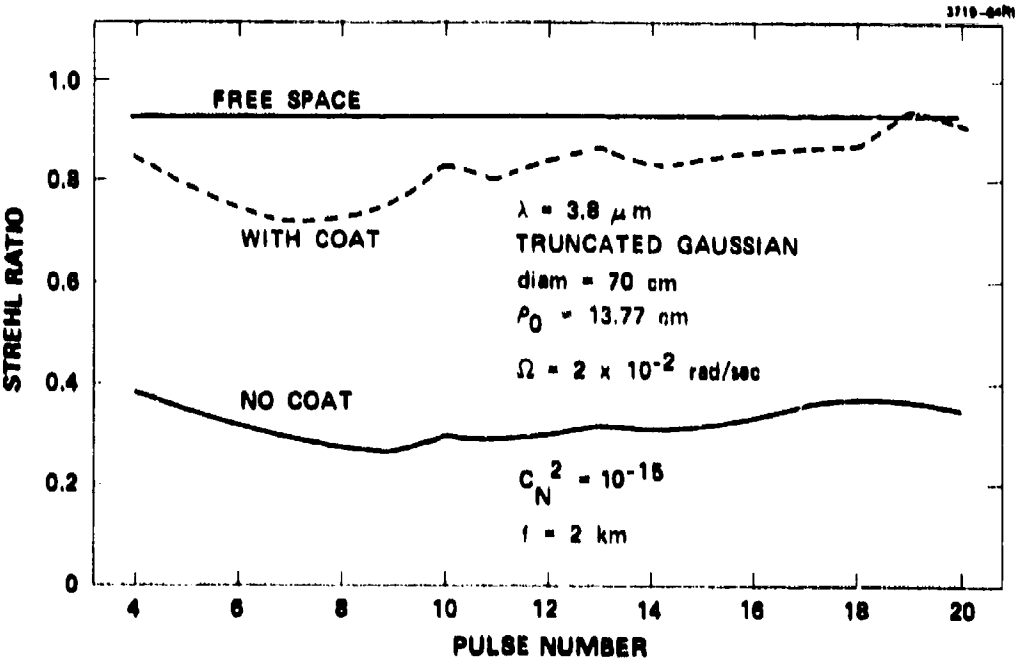

Fig. 4.14. Phase conjugate compensation of turbulence effects versus time (no thermal blooming).

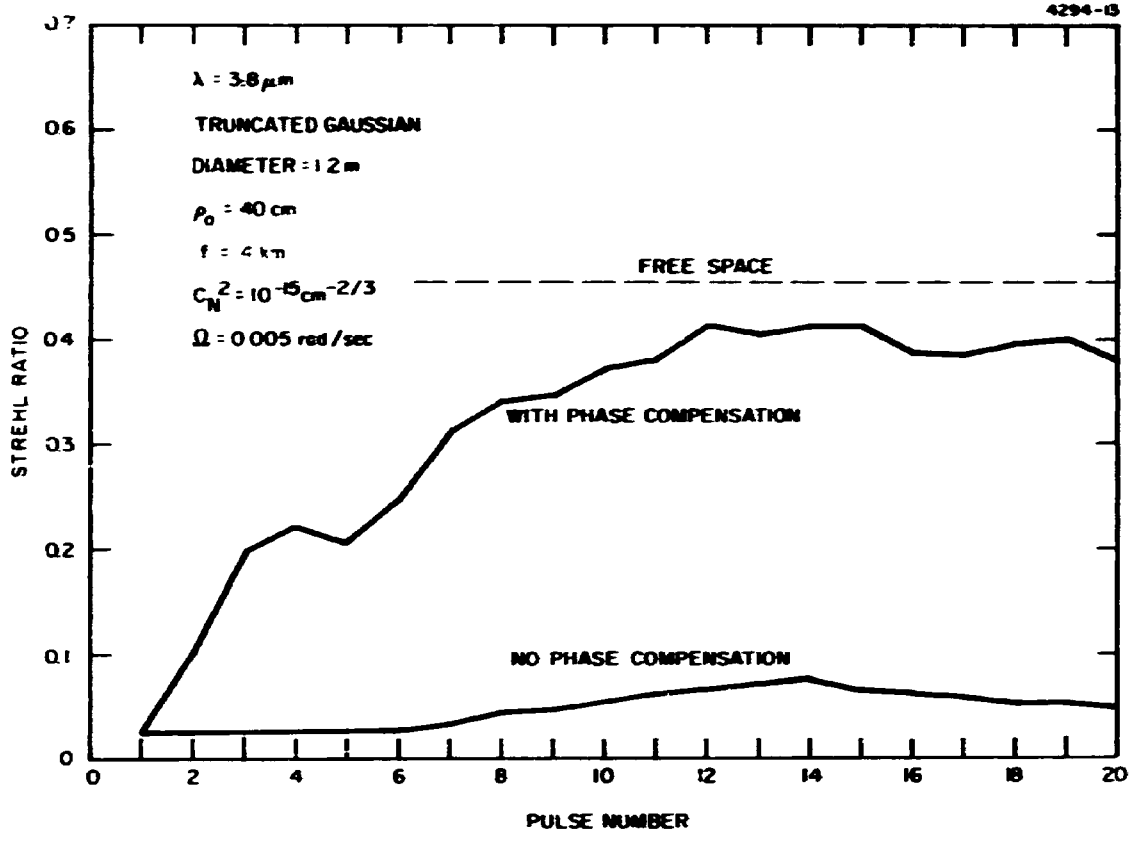

Fig. 4.15. Phase conjugate compensation of turbulence effects versus time (no thermal blooming).

train the return comes from a more extended portion of the target because of the broadness of the transmitted beam and the very significant fluctuation in the amplitude of that beam in the target plane.

Results for phase conjugate correction of the combined effects of turbulence and thermal blooming are shown in Figs. 4.16 and 4.17. The results in Fig. 4.16 apply to a truncated gaussian beam with an e-folding radius of 23 cm and a truncation circle diameter of 70 cm. This beam is being slewed at 20 mrad/sec. The results in Fig. 4.17 pertain to a truncated gaussian beam with an e-folding radius of 40 cm and a truncation circle diameter of 1.2 m (same degree of truncation as the 70 cm beam used in Fig. 21). This beam is being slewed at only 5 mrad/sec. In addition to demonstrating the ability of phase conjugate adaptive systems to achieve substantial corrections for the effects of turbulence, these results illustrate the advantage of using large beams in thermal blooming situations. Even though the slew rate in Fig. 4.17 is four times slower than that in Fig. 4.16, the peak irradiance obtained without correction is increased by a factor of five. Likewise, the peak irradiance obtained in Fig. 4.17 with phase conjugate correction is increased by a factor of three beyond the comparable result obtained in Fig. 4.16. This improvement in peak irradiance can be attributed to the increased size of the beam used in Fig. 4.17 (1.2 m optics versus 70 cm optics).

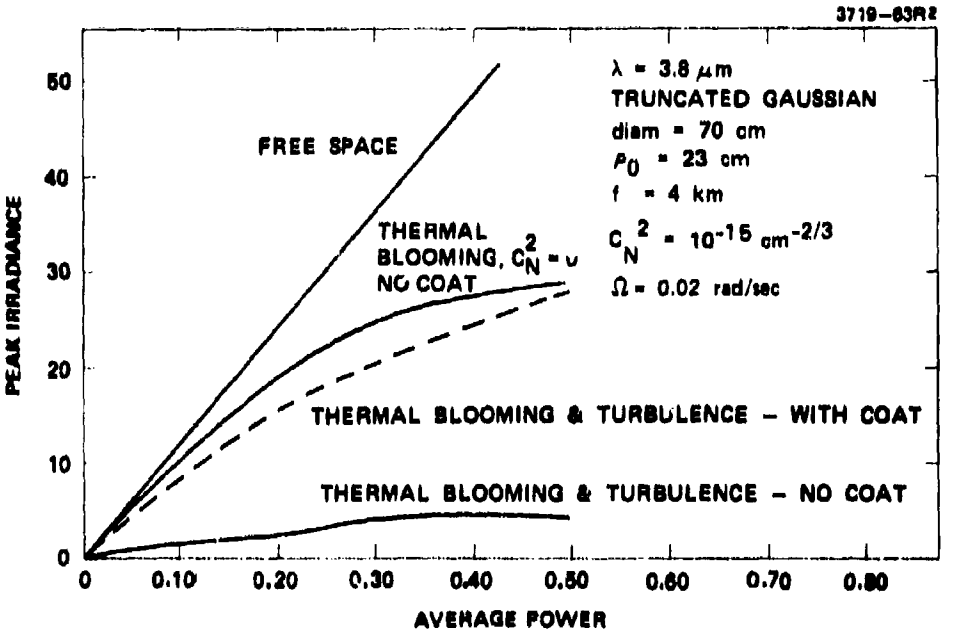

Fig. 4.16. Phase conjugate compensation at 3.8 μm, 70 cm beam.

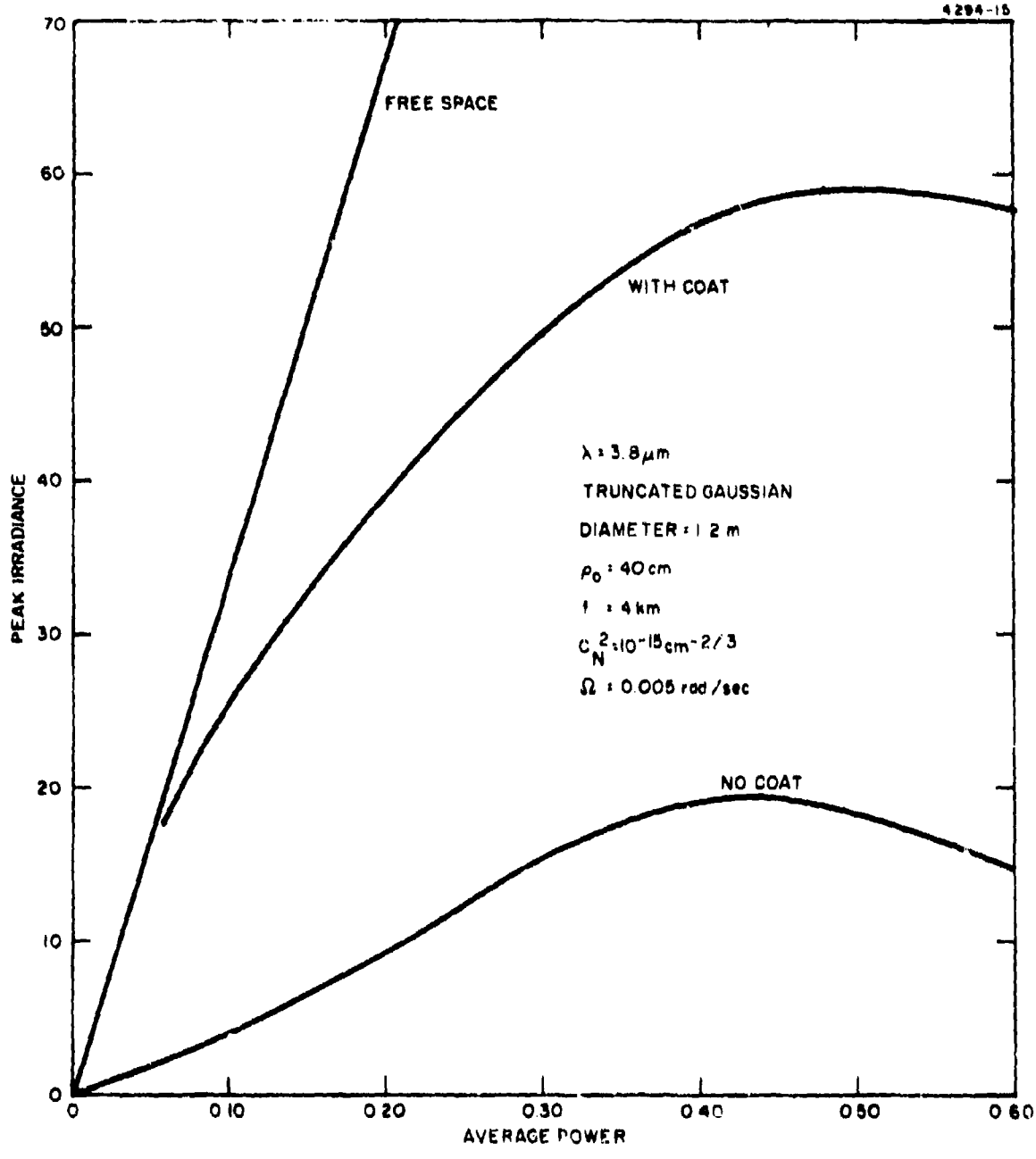

Fig. 4.17. Phase conjugate compensation at 3.8 um, 1.2 m beam.

V. CONCLUSIONS AND RECOMMENDATIONS

5.1 Conclusions

The most important conclusion that we have reached on the basis of the work done on this contract is that adaptive optical systems employing any of the various types of return-wave control algorithms are not likely to yield very significant compensation for the effects of cw thermal blooming unless the target scattering occurs over regions having extent considerably smaller than the diffraction-limited beam size. As a matter of fact, some of the data we have obtained indicate that under some conditions such adaptive systems may actually decrease target irradiance instead of increasing it. The analysis in Section 2.1 of this report indicates that the problem with the return-wave control algorithm originates from the fact that it inherently tends to use the conjugate of the phase of the field returned from the target as the phase correction. This phase conjugate control policy works well as long as the target acts as a point scatterer or a discrete collection of such scatterers. However, if the scattering originates from extended scatterers rather than point scatterers, there is an isoplanatic-type of effect wherein the return phase becomes garbled by the interference between returns from the various parts of the scatterer. This isoplanatic effect is of no consequence for most turbulence compensation situations since the isoplanatic area is usually larger than the principal scattering region. Hence, return-wave systems yield good compensation for turbulence effects. For cw thermal blooming, however, our computer results indicate that the isoplanatic region is smaller than the diffraction-limited spot size. We base this conclusion on the fact that very little compensation was obtained for cw thermal blooming effects with glints having an extent approximately equal to the diffraction-limited spot size.

It should be noted that the above conclusions apply to any adaptive optical system employing a return wave-type of control algorithm, not just the explicit phase conjugate-type of system. As discussed in Section II, this includes systems that operate by maximizing some functional of the irradiance distribution obtained by imaging the target; e.g., maximization of the energy through a pinhole for a point glint target or maximizing the "sharpness" of an image of an extended target.

With regard to turbulence compensation, we have found that return-wave adaptive optical systems yield significant corrections. Typically, it is possible to obtain almost diffraction-limited target intensities even for relatively strong turbulence. The amount of improvement is particularly impressive at 3.8 μm where the turbulence degradation is quite severe without adaptive compensation; e.g., we have obtained a factor of seven increase in peak target irradiance for a 70 cm diameter, 3.8 μm beam propagated over a 4 km path having a turbulence level equivalent to an index structure constant of $C_N^2 = 10^{-15}$ $cm^{-2/3}$ (moderate turbulence on a low altitude path).

In the results discussed above, and in all the other results in which the full propagation simulation was used, we have not simulated the effect of having fewer mirror actuators than mesh points. We have simply equated the phase correction to the conjugate of the return wave on a mesh-point-by-mesh-point basis. However, we have obtained quantitative estimates of the degrading effect of having fewer actuators than mesh points from both theoretical analysis and a simplified computer simulation in which the effect of turbulence was represented by a single phase screen placed in front of the transmitter (see Section 4.2 for details). Using the theory developed in Section 4.2.2, which yields results that agree well with the computer simulation results,

we obtain the following condition on the number of actuators per unit area of mirror surface required to yield a Strehl ratio of .9 or greater (i.e., the degradation in Strehl ratio due to the finite number of mirror actuators is < .10)

$$\left|\begin{array}{l}\text{Number of Actuators}\\ \text{Required per Unit}\\ \text{Area}\end{array}\right| \geq .529(k^2\, C_N^2\, z)^{6/5} \qquad (5.1)$$

We estimate, for example, that approximately .037 actuators per cm^2 of primary mirror area are required to yield results comparable to the mesh-point-by-mesh-point results for the 3.8 μm case cited above, i.e., approximately 143 actuators are required for 70 cm optics.

In the case of multipulse propagation, we have found that adaptive optical systems employing return wave-type of control algorithms can significantly increase the target irradiance in thermal blooming situations. The amount of correction attained varies depending on the conditions but can approach a factor of three in some cases. The reason for the significantly better correction obtained for multiple pulse thermal blooming effects is principally that the distorting effect of the thermal blooming tends to move back away from the target and closer to the transmitter. This has the effect of increasing the isoplanatic area at the target and thus alleviates the problem that occurs with cw thermal blooming.

Although we have not yet obtained computer simulation results for an adaptive optical system employing an outgoing-wave multidither control algorithm, we have developed an approach to the problem. This approach is a modified version of what has been done at Lincoln Laboratory by Herrmann and Bradley. Since an outgoing-wave multidither control algorithm is basically a maximization process, it can be represented by a function maximization routine. In contrast to the

Lincoln Laboratory work in which the target irradiance was directly maximized with respect to the phase correction, we recommend a simulation which more closely models the operation of an actual adaptive optical system. To accomplish this, we would use a time-dependent propagation code and would maximize the integrated irradiance of the field returned to the transmitter from the target. There are two principal differences between this approach and that taken by Lincoln Laboratory. First, we would maximize the integrated irradiance of the field returned from the target rather than the target irradiance directly. This will allow us to determine the sensitivity of the maximization process to the size of the receiver and the nature of the target glint. Secondly, use of the time-dependent code will allow us to determine whether the instantaneous maximum provided by an outgoing-wave multi-dither algorithm yields a long-term global maximum irradiance at the target or instead simply yields a secondary maximum. Put in another way, we would be able to determine whether it is possible to end up at a local (secondary) maximum rather than the global maximum when we instantaneously maximize the integrated irradiance of the return field; i.e., could we have reached a higher maximum had we taken a different path in time (via a different control policy)?

5.2 Recommendations

Dividing the subjects again on the basis of the type of control algorithm used, we recommend the following additional work on the adaptive optics simulation problem:

Return Wave Systems — Generally, more data are needed for a broader set of system, atmospheric, and target parameters than have been investigated to this date. These parameters include the mirror diameter, type of mirror (segmented or deformable), number of actuators, initial

irradiance distribution (including distributions typical of actual high power lasers), target range and slew rate, and target glint size. Of particular importance in the cw thermal blooming problem is the investigation of the degree of compensation achievable as a function of target glint size. These results should be correlated with known properties of real targets in order to arrive at an authoritative assessment of the effects of target glint size on return-wave systems.

Outgoing-Wave Multidither Systems — As indicated earlier, we recommend that such systems be simulated by a function maximization routine in conjunction with a time-dependent propagation code. Initially, at least, the main intent of such a simulation should be to establish whether an outgoing-wave multidither system yields a truly global maximization for the irradiance at the target or instead yields simply a secondary maximum. The effect of target glint size and receiver size on the maximization process will be of particular interest in these studies. Other parameters that should be varied are mirror diameter, type of mirror, number of actuators, initial irradiance distribution, and target range and slew rate.

REFERENCES

1. R. A. Muller and A. Buffington, J. Opt. Soc. Am. 64, 1200 (1974).

2. L. C. Bradley and J. Herrmann, Appl. Opt. 13, 331 (1974).

3. W. B. Bridges et al., "Coherent Optical Adaptive Techniques (COAT)," Technical Report No. 2, Contract No. F30602-73-C-0248, 1973.

4. R. J. Roark, Formulas for Stress and Strain (McGraw-Hill, New York, 1968).

5. W. P. Brown, J. Opt. Soc. Am. 61, 1051 (1971).

6. D. L. Fried, J. Opt. Soc. Am. 56, 1372 (1966).

APPENDIX A

RECIPROCITY CONSIDERATIONS

The equivalence of the transmitting and receiving patterns of an antenna is a consequence of a general reciprocity relation satisfied by the solution of the Maxwell equations. For the propagation problems of concern in this report, the solution of the Maxwell equations can be derived from the solution of a reduced wave equation. The desired reciprocity relation is obtained by considering the case where there is a delta source located at one of two points $\underline{x}_i$ ($i = 1,2$) within a volume V bounded by a surface S

$$\left[\nabla^2 + k^2 n^2(\underline{x})\right] u_i(\underline{x}) = \delta(\underline{x} - \underline{x}_i) \qquad (A.1)$$

We assume that the refractive index distribution within V and the boundary conditions on S are independent of the location of the source. If we multiply the equation for $u_1(\underline{x})$ by $u_2(\underline{x})$ and that for $u_2(\underline{x})$ by $u_1(\underline{x})$, subtract the results, and integrate over V, we obtain

$$\int_S dS \left(u_2 \frac{\partial u_1}{\partial n} - u_1 \frac{\partial u_2}{\partial n}\right) = u_2(\underline{x}_1) - u_1(\underline{x}_2) \qquad (A.2)$$

The surface integral is obtained by applying Green's theorem to the volume integral of $u_2 \nabla^2 u_1 - u_1 \nabla^2 u_2$.

For a wide range of problems, including those of interest in this report, we can approximate the boundary conditions on S by the impedance boundary condition

$$\left(\frac{\partial}{\partial n} + \sigma\right) u_i = 0, \qquad \underline{x} \text{ on } S \qquad (A.3)$$

where σ is a constant that depends on the surface impedance

of the boundary. Hence, the surface integral in Eq. (A.2) is zero and we obtain the following reciprocity relation

$$u_1(\underline{x}_2) = u_2(\underline{x}_2) \tag{A.4}$$

This relation states that the field produced at $\underline{x}_2$ by a source at $\underline{x}_1$ is the same as the field produced at $\underline{x}_1$ by a source at $\underline{x}_2$. We note that the derivation of Eq. (A.4) did not require any assumptions regarding the nature of the refractive index function $n(\underline{x})$ in Eq. (A.1). Hence, the reciprocity relation we have derived is valid regardless of the state of homogeneity of the medium between $\underline{x}_1$ and $\underline{x}_2$.

To prove the equivalence of the transmitting and receiving patterns of an antenna immersed in an inhomogeneous medium, we need now merely consider the situation shown in Fig. A.1. The antenna is depicted here as a lens. According to the reciprocity relation given in Eq. (A.4), the field radiated to the point $\underline{x}_2$ from a point source at $\underline{x}_1$ behind the lens is equal to the field received at $\underline{x}_1$ from a point source at $\underline{x}_2$. This implies that the transmitting and receiving patterns of the lens are the same because, as shown in Fig. A.1, the field at $\underline{x}_1$ in the receiving case bears the same geometrical relationship to the center of the receiving pattern (indicated by the dashed lines in Fig. A.1), as does the field at $\underline{x}_2$ to the center of the transmitted pattern (indicated by the double-dashed line in Fig. A.1).

As a corollary to the equivalence between the transmitting and receiving patterns of an antenna, we note that if one images a point source located at $\underline{x}_2$, the point of maximum irradiance in the image plane is the ideal place to locate a point source if it is desired to deliver maximum power to $\underline{x}_2$ on transmit. To prove this, we recall from Eq. (A.4) that the field at $\underline{x}_2$ radiated by a source at $\underline{x}_1$ is the same as that which occurs when the source and observation points

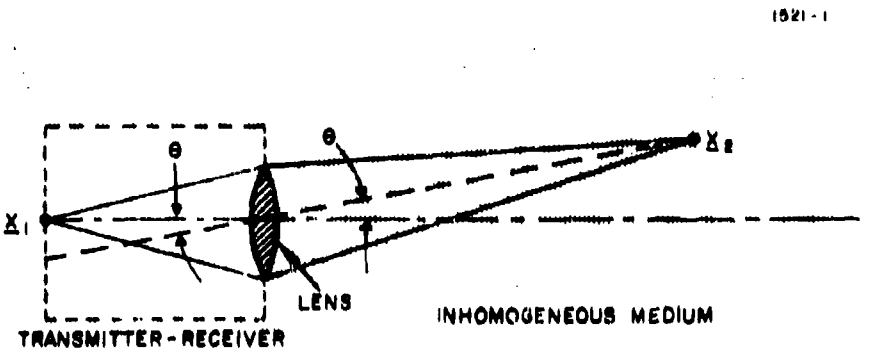

Fig. A.1. Antenna pattern reciprocity.

are interchanged. Hence, the fact that we locate the point source at the point of maximum irradiance from the source at $\underline{x}_2$ implies that the field radiated to $\underline{x}_2$ will be maximized because the transmitting and receiving patterns of the antenna are equivalent and a point source located at the maximum of one pattern will likewise produce at maximum at the reciprocal point. Basically, we are saying that maximum power is delivered to $\underline{x}_2$ when the transmitter is pointed at the apparent position of $\underline{x}_2$. This result has wide application in communication and radar systems where it is often necessary to deliver energy to a point specified by an imaging system.

In addition to the equivalence between the transmitting and receiving patterns of an antenna and the pointing corollary discussed above, the reciprocity relation given in Eq. (A.4) has the obvious consequence that the fluctuations of a spherical wave propagating in a random medium are reciprocal regardless of whether the random inhomogeneities are spatially homogeneous. By reciprocal we mean that the fluctuations at a point $\underline{x}_2$ in the field radiated from a spherical wave source at a point $\underline{x}_1$ are the same as those observed at $\underline{x}_1$ when the spherical source is at $\underline{x}_2$. This means, for instance, that earthbound measurements of the fluctuations of a spherical wave emanating from a point source outside the earth's atmosphere can be used to predict the fluctuations that would occur in the reciprocal situation; namely, an earthbound point source radiating to the same point in space.

Unfortunately, the reciprocal relation between the fluctuations of the spherical wave fields in random media generally does not apply to the fluctuations of fields radiated by more complicated source. For example, consider the source-medium configuration shown in Figs. A.2a and b. The source in this figure is composed of a point source, lens combination, which is generically equivalent to most laser source. With this type of source we change the location of the lens when

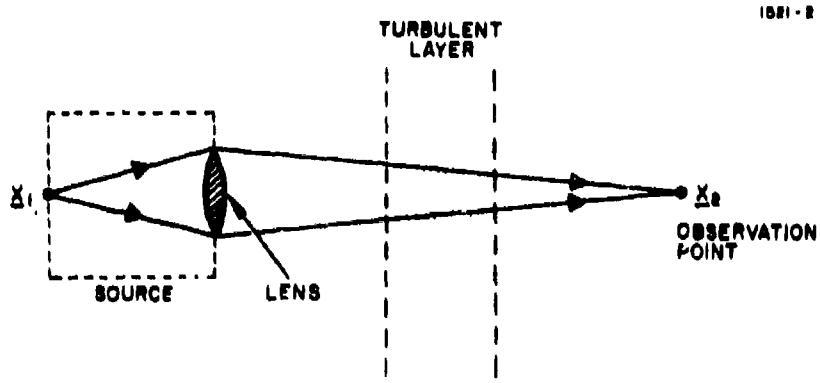

a. SOURCE AT $\underline{x}_1$, OBSERVER AT $\underline{x}_2$

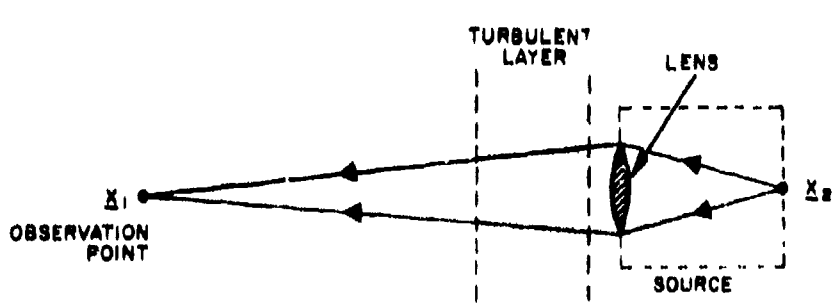

b. SOURCE AT $\underline{x}_2$, OBSERVER AT $\underline{x}_1$

Fig. A.2. Non-reciprocal configurations.

the source and observation points are interchanged. In effect, this means that the refractive index function $n(\underline{x})$ in Eq. (A.1) is not the same when the "source" is at $\underline{x}_1$, as it is when the "source" is at $\underline{x}_2$. Consequently, the terms involving the refractive index do not completely cancel when we follow the procedure outlined earlier for the derivation of the reciprocity relation, given in Eq. (A.4). There is an additional term in Eqs. (A.2) and (A.4) that destroys the simple reciprocal relationship that exists for point source fields.

END